

Manuscript version: Author's Accepted Manuscript

The version presented in WRAP is the author's accepted manuscript and may differ from the published version or Version of Record.

Persistent WRAP URL:

<http://wrap.warwick.ac.uk/158740>

How to cite:

Please refer to published version for the most recent bibliographic citation information. If a published version is known of, the repository item page linked to above, will contain details on accessing it.

Copyright and reuse:

The Warwick Research Archive Portal (WRAP) makes this work by researchers of the University of Warwick available open access under the following conditions.

© 2021, Elsevier. Licensed under the Creative Commons Attribution-NonCommercial-NoDerivatives 4.0 International <http://creativecommons.org/licenses/by-nc-nd/4.0/>.



Publisher's statement:

Please refer to the repository item page, publisher's statement section, for further information.

For more information, please contact the WRAP Team at: wrap@warwick.ac.uk.

A NEW DAMAGE FACTOR FOR SEISMIC ASSESSMENT OF DEFICIENT BARE AND FRP- RETROFITTED RC STRUCTURES

George Markou^{*1,3},

Reyes Garcia^{2a},

Christos Mourlas^{4b},

Maurizio Guadagnini^{3c},

Kypros Pilakoutas^{3d},

Manolis Papadrakakis^{4e}

¹Department of Civil Engineering, University of Pretoria, South Africa

²School of Engineering, The University of Warwick, UK

³Department of Civil and Structural Engineering, The University of Sheffield, UK

⁴Department of Civil Engineering, National Technical University of Athens, Greece

ABSTRACT

The seismic assessment of reinforced concrete (RC) structures before and after retrofitting is a challenging task, mainly because existing numerical tools cannot accurately model the evolution of concrete damage. This article proposes an innovative numerical method suitable to model and assess the ultimate carrying capacity of RC structures. The modelling approach proposes a steel constitutive material model with a damage factor that accounts for accumulated damage within the surrounding concrete domain, which effectively captures bar slippage. The proposed method is validated with experimental results from full-scale cyclic tests on deficient bare and CFRP-retrofitted RC joints tested previously by the authors. The results indicate that the proposed simulation method captures the extreme nonlinearities observed in the tested RC joints, with acceptable accuracy and computational robustness. The results of this study are expected to contribute towards the development of more reliable numerical tools and design guidelines for efficient seismic assessment of RC

*Corresponding Author, Associate Professor, E-mail: george.markou@up.ac.za, g.markou@sheffield.ac.uk

^aAssistant Professor: reyes.garcia@warwick.ac.uk

^bPh.D., E-mail: mourlasch@central.ntua.gr

^cSenior Lecturer: m.guadagnini@sheffield.ac.uk

^dProfessor, E-mail: k.pilakoutas@sheffield.ac.uk

^eProfessor, E-mail: mpapadra@central.ntua.gr

structures before and after earthquakes.

Keywords: Beam-column RC joints; Finite Element Modelling; FRP strengthening; Bar Slippage; Cyclic Nonlinear Analysis.

1. Introduction

Many seismically active countries have large numbers of reinforced concrete (RC) structures that were designed either using old design codes or without accounting for seismic loads. Post-earthquake missions have revealed that critical elements of such structures (e.g. columns and beam-column joints) had insufficient shear reinforcement and inadequate bar anchorage lengths, which led to structural collapses and consequently to huge human and economical losses [1]. To minimise damage and human/economical losses during earthquakes, engineers utilise assessment and retrofitting techniques that, nowadays, are incorporated into modern seismic codes.

Over the last decades, engineers have also developed practical numerical and computational tools to seismically assess existing RC structures. However, such assessments before and after retrofitting are challenging, mainly because a) the progression of concrete damage and b) the effect of the retrofitting intervention are difficult to capture by existing models and simulation software. To address these drawbacks, the authors have recently proposed a new Hybrid Modelling (HYMOD) approach that provides numerically objective, accurate, and computationally robust solutions to the assessment of the ultimate carrying capacity of retrofitted structures [2]. The approach proved effective in modelling the seismic behaviour of a 4-storey RC building [3] subjected to pseudo-dynamic tests in bare and retrofitted conditions for which experimental data were available. The RC building was retrofitted with RC infill walls and Carbon Fibre Reinforced Polymer (CFRP) jackets at its base. 8-noded hexahedral elements were used to discretize the shear-dominated concrete domain, whereas the reinforcement was modelled with embedded beam elements. Furthermore, beams and columns that are expected to be bending dominated, were discretized with beam-column finite elements. The numerical results presented in [3] captured accurately the experimentally-derived base shear. However, pinching effects were not well captured because concrete material deterioration and

potential bar slippage at the building base were not incorporated into the adopted constitutive material models of steel and concrete.

Previous studies have proposed several models that attempt to capture extreme nonlinear RC structural behaviour under cyclic conditions. Lykidis and Spiliopoulos [4] proposed a 3D detailed modelling approach that uses 20-noded hexahedral elements to treat cracking with the smeared crack method and discretised reinforcement with embedded rod elements. The model in [4] included an additional degree of freedom (dof) per embedded bar to account for slippage. Although Lykidis and Spiliopoulos' model captured accurately the experimental results of a corner beam-column RC joint that exhibited slippage and concrete damage, the model did not capture pinching when used to simulate the behaviour of internal RC joints. This can be attributed to the inability of the concrete and steel material models to capture accumulated damage due to crack opening and closing during cyclic loading, and to numerically predict the effect of bar slippage on the overall behaviour of the joints.

Previous studies have also proposed a number of numerical modelling approaches to simulate the behaviour of retrofitted RC bridges and framed structures [5-9] under monotonic loading. In addition to that, extensive research work on modeling of strengthened RC beams was presented in [10-14], while more recent publications on this field were discussed in [14-18]. Nonlinear finite element investigations were also performed on prestressed beams [19-20] and composite beam [21] under monotonic loading conditions. Furthermore, significant work has been done on RC joints [22-28] retrofitted with FRP laminates, where numerical models were utilized to investigate the mechanical behaviour of beam-column connections.

In addition to the above, research work on numerical modeling of retrofitted RC columns was performed in [29-31] in an attempt to develop models that would capture the nonlinear mechanical behaviour of retrofitted vertical structural members. Masonry structures were also considered [32-33], while retrofitted RC ties were investigated in [34]. Nevertheless, none of these studies proposed models that can capture the cyclic behaviour of retrofitted structural members. On the other hand, Cortés-Puentes and Palermo [35] investigated the cyclic behavior of RC shear walls strengthened with different CFRP configurations. The numerical analyses were carried out using the 2D finite element

software VecTor2. Whilst the numerical results predicted well the experimental load-deformation loops, the modelling approach is only applicable to 2D problems.

Mourlas et al. 2019 [36] extended the work in [37, 38] to carry out 3D nonlinear cyclic analysis and proposed the use of two material damage factors in order to take into account the effect of opening and closing of cracks within a concrete hexahedral finite element that captures cracking using the smeared crack approach. The results in [36] confirmed that the proposed integration of the concrete and steel material models with the respective damage factors predicted very well the static and dynamic nonlinear behaviour of concrete structures with pinching. The modelling method proposed in [36] captured the cyclic behaviour of RC structures with pinching without the need of introducing additional dofs that would have made computations more intensive.

In this work, the material model of steel, as presented in [36], was integrated with a new reduction factor, which is defined by the accumulated damage of crack opening/closing, in order to reduce the stiffness of the steel reinforcement in the cracked concrete regions within which slippage is expected to occur. This article investigates the ability of the proposed material model to capture the overall mechanical response of severely damaged concrete joints characterized by intense pinching phenomena. The proposed modelling method is validated with results of bare and retrofitted RC joints tested previously by the authors. Section 3 presents a brief description of the experimental programme reported in [39]. Both phases are modelled and analysed in Section 4. Conclusions and future work are given in Section 5.

2. Material Modelling

This section introduces the concrete and steel material models, as well as the new damage factors. The proposed material model is based on the triaxial behaviour of concrete taking into account the effect of opening and closing of cracks, in order to capture strength and stiffness degradation, and pinching effects.

2.1 Concrete Material Modelling and Damage Factor

The constitutive modelling of concrete is an extension of the Kotsovos and Pavlovic [40] model as

it is described in [37]. The constitutive relations take the following form:

$$\varepsilon_0 = \varepsilon_{0(h)} + \varepsilon_{0(d)} = (\sigma_0 + \sigma_{id}) / (3K_s) \quad (1)$$

$$\gamma_0 = \gamma_{0(d)} = \tau_0 / (2G_s) \quad (2)$$

where K_s and G_s are the secant forms of bulk and shear moduli, respectively. The secant forms of bulk, shear modulus and σ_{id} are expressed as functions of the current state of stress, which were derived by regression analysis of experimental data [40]. Based on the regression analysis, the following secant forms of bulk and shear moduli derived:

$$K_s = \frac{1}{3} \frac{\sigma_0}{\varepsilon_0}, \quad G_s = \frac{1}{2} \frac{\tau_0}{\gamma_0} \quad (3)$$

In addition to the above, the formulae that describe the relationship between the secant bulk and shear moduli with the initial bulk (K_e) and shear (G_e) moduli are given in Eqs. 4 and 5.

$$\frac{K_s}{K_e} = \frac{1}{1 + A \left(\frac{\sigma_0}{f_c} \right)^{b-1}} \quad \text{for } \sigma_0 / f_c \leq 2 \quad (4a)$$

$$\frac{K_s}{K_e} = \frac{1}{1 + 2^{b-1} A b - 2^b A \left(\frac{\sigma_0}{f_c} \right)^{-1}} \quad \text{for } \sigma_0 / f_c \leq 2 \quad (4b)$$

$$\frac{G_s}{G_e} = \frac{1}{1 + C \left(\frac{\tau_0}{f_c} \right)^{d-1}} \quad (5)$$

where,

$$b = 2.0 + 1.81 \cdot 10^{-8} \cdot f_c^{4.461} \quad (6)$$

$$d = 2.12 + 0.0183 \cdot f_c \quad \text{for } f_c \leq 31.7 \text{ MPa} \quad (7a)$$

$$d = 2.70 \quad \text{for } f_c > 31.7 \text{ MPa} \quad (7b)$$

and where A is given by:

$$A = 3a_c K_e f_c^{b-1} \quad (8)$$

By performing a regression analysis on the experimental data [40], the following formulae for

parameter A, where obtained:

$$A = 0.516 \quad \text{for } f_c \leq 31.7 \text{ MPa} \quad (9)$$

$$A = \frac{0.516}{1 + 0.0027(f_c - 31.7)^{2.389}} \quad \text{for } f_c > 31.7 \text{ MPa} \quad (10)$$

Furthermore, the calculation of the stress σ_{id} is performed through an expression that is also derived from a regression analysis through the use of the experimental data presented in [40]:

$$\frac{\sigma_{id}}{f_c} = M \left(\frac{\tau_0}{f_c} \right)^n \quad (11)$$

$$M = \frac{k}{1 + l \left(\frac{\sigma_0}{f_c} \right)^m} \quad (12)$$

$$k = \frac{4.0}{1 + 1.087 \cdot (f_c - 15.0)^{0.23}} \quad (13)$$

$$l = 0.222 + 0.01086 \cdot f_c - 0.000122 \cdot f_c^2 \quad (14)$$

$$m = -2.414 \quad \text{for } f_c \leq 31.7 \text{ MPa} \quad (15)$$

$$m = -3.532 + 0.0352 \cdot f_c \quad \text{for } f_c > 31.7 \text{ MPa} \quad (16)$$

$$n = 1.0 \quad \text{for } f_c \leq 31.7 \text{ MPa} \quad (17)$$

$$n = 0.3124 + 0.0217 \cdot f_c \quad \text{for } f_c > 31.7 \text{ MPa} \quad (18)$$

The model adopts a smeared crack approach (see Fig. 1) by simulating a geometrical discontinuity with the assumption of displacement continuity. The crack opening strategy during each load increment foresees the use of the unified total crack approach (UTCA) proposed by Lykidis and Spiliopoulos [4], which assumes that the state of crack formation or closure is treated in a unified way within every Newton-Raphson internal iteration. When a crack opens, the material properties normal to the crack plane are set to zero. The concrete material assumes that it loses all of its carrying capacity along the vertical direction of the crack, where it behaves in a brittle manner. The expression of the strength envelope of concrete is provided in Eq. 19 and it is based on the Willam and Warnke [41]

formulae:

$$\tau_{0u} = \frac{2\tau_{0c}(\tau_{0c}^2 - \tau_{0e}^2)\cos\theta + \tau_{0c}(2\tau_{0e} - \tau_{0c})\sqrt{4(\tau_{0c}^2 - \tau_{0e}^2)\cos^2\theta + 5\tau_{0e}^2 - 4\tau_{0c}^2\tau_{0e}^2}}{4(\tau_{0c}^2 - \tau_{0e}^2)\cos^2\theta + (2\tau_{0e} - \tau_{0c})^2} \quad (19)$$

where the rotational variable θ defines the deviatoric stress orientation on the octahedral plane; τ_{0e} ($\theta=0^\circ$) and τ_{0c} ($\theta=60^\circ$) correspond to the state of $\sigma_1=\sigma_2>\sigma_3$ (triaxial extension) and $\sigma_1>\sigma_2=\sigma_3$ (triaxial compression), respectively, and are expressed analytically. These expressions are obtained by triaxial experimental tests as described in [40].

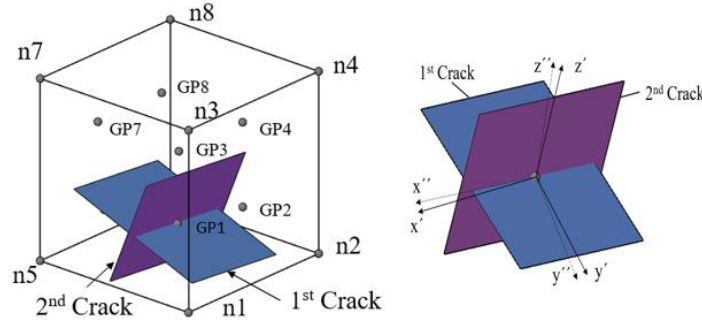


Figure 1: Local axes for the case of two cracks at a specific Gauss point [36].

The material model uses a flexible crack closing criterion, introduced in Mourlas et al. [36]. This numerical criterion was critical in achieving a faster convergence ratio during the cyclic load analysis. Accordingly, the closure of cracks is expressed as:

$$\varepsilon_i \leq \left(b - \frac{n_{cr} - 1}{n_{tot}} \right) \cdot \varepsilon_{cr} \quad (20)$$

where ε_i is the current strain in the i -direction that is normal to the crack plane; ε_{cr} is the strain that causes cracking formation; b is the number of the imposed displacement branch of the load history; n_{cr} is the number of increments that the crack is formed at and n_{tot} is the total number of increments that an imposed displacement branch is divided into.

When the criterion of crack-closure is satisfied at a Gauss Point (GP) that had only one prior crack formation, part of the stiffness is lost along the previous crack plane (material deterioration) assumed to form in an orthogonal direction to the maximum principle tensile stress. Therefore, the constitutive matrix takes the following form:

$$C_l^* = \begin{bmatrix} a_n \cdot (1-D_c) \cdot (2G_t + \mu) & a_n \cdot (1-D_c) \cdot \mu & a_n \cdot (1-D_c) \cdot \mu & 0 & 0 & 0 \\ a_n \cdot (1-D_c) \cdot \mu & 2G_t + \mu & \mu & 0 & 0 & 0 \\ a_n \cdot (1-D_c) \cdot \mu & \mu & 2G_t + \mu & 0 & 0 & 0 \\ 0 & 0 & 0 & a_s \cdot (1-D_c) \cdot \beta \cdot G_t & 0 & 0 \\ 0 & 0 & 0 & 0 & a_s \cdot (1-D_c) \cdot \beta \cdot G_t & 0 \\ 0 & 0 & 0 & 0 & 0 & a_s \cdot (1-D_c) \cdot \beta \cdot G_t \end{bmatrix} \quad (21)$$

where β is a shear retention factor; and a_n and a_s are constants with values of 0.25 and 0.125, respectively, based on the parametric investigation presented in [36].

The proposed expressions of the constitutive matrix describe the anisotropic behaviour of concrete at the local coordinate system. Therefore, it has to be transformed into the global system using the standard coordinate system transformation laws:

$$C_g = T^T C_l T \quad (22)$$

where T is the transformation matrix consisting the direction cosines that define the relative orientation of the local to global axis; D_c is a damage factor proposed in [36] that describes the accumulated energy loss due to the number of times a crack has opened and closed. D_c is calculated as follows [36]:

$$D_c = e^{-\left(1-a\right)/f_{cc}} = e^{-\left(1-\left(1-\frac{\varepsilon_{cr}}{\varepsilon_{max}}\right)\right)/f_{cc}} = e^{-\left(\frac{\varepsilon_{cr}}{\varepsilon_{max}}\right)/f_{cc}} \quad (23)$$

where f_{cc} is the number of times where a crack has closed and is updated in every iteration at every GP. Fig. 2 shows the variation of D_c (Eq. 23) as a function of the parameter a and f_{cc} .

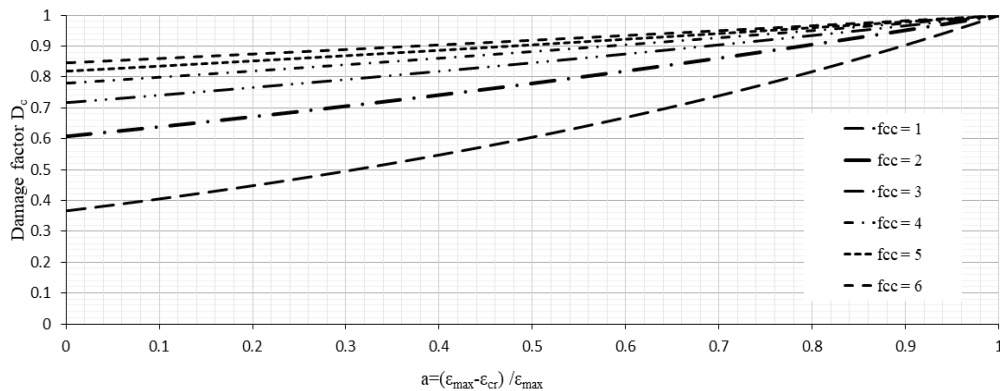


Figure 2: Schematic representation of the damage factor D_c (Eq. 23) as a function of the parameter a and f_{cc} [36].

During nonlinear analysis, the constitutive matrix is calculated from Eq. 21 when a crack is closed

at a GP that previously had one or two cracks. After crack closure, the stresses are corrected through the use of the following expression:

$$\sigma^i = \sigma^{i-1} + C_g \cdot \Delta \varepsilon^i \quad (24)$$

Finally, once all cracks have closed (at a previously cracked GP) and the reduction factor a (in Eq. 23) of one of the previous cracks is larger than 0.5, the constitutive matrix takes the following form:

$$C_g' = (1 - D_c) \cdot C_g \quad (25)$$

As an additional step and in an attempt to introduce a stabilizing factor during cyclic modelling of extremely cracked concrete regions that were studied in this research work and presented in Section 4, the modification of the constitutive matrix of a fully crushed GP is proposed to take the following form:

$$C_l' = \begin{bmatrix} \beta_c \cdot (1 - D_c) \cdot (2G_t + \mu) & 0 & 0 & 0 & 0 & 0 \\ 0 & \beta_c \cdot (1 - D_c) \cdot (2G_t + \mu) & 0 & 0 & 0 & 0 \\ 0 & 0 & \beta_c \cdot (1 - D_c) \cdot (2G_t + \mu) & 0 & 0 & 0 \\ 0 & 0 & 0 & \beta_c \cdot (1 - D_c) \cdot \beta \cdot G_t & 0 & 0 \\ 0 & 0 & 0 & 0 & \beta_c \cdot (1 - D_c) \cdot \beta \cdot G_t & 0 \\ 0 & 0 & 0 & 0 & 0 & \beta_c \cdot (1 - D_c) \cdot \beta \cdot G_t \end{bmatrix} \quad (26)$$

where $\beta_c = 0.025$, a parameter similar to the shear retention factor β and D_c is the damage factor from Eq. 23. The GP is assumed to have lost its resistance, after it crushed [36], but due to the newly developed constitutive matrix of Eq. 26, it is now assumed that it has the ability to develop a resistance that is decreasing as the compressive cracks are increasing. Therefore, the cracks of a crushed GP cannot close, but do maintain a low stiffness, which was found to introduce numerical stability when excessive cracking occurs. This remaining stiffness resistance is necessary when dealing with modelling RC structures that are subjected to high axial compressive loading or joints that develop excessive diagonal cracks or intense concrete spalling.

2.2 Steel Material Modelling and Modified Damage Factor

The level of damage that occurs due to the opening of cracks also affects the bond between steel reinforcement and the surrounding concrete. Consequently, this damage mechanism directly affects

the force transfer between the steel reinforcement to the surrounding concrete domain, especially in the anchorage areas. Therefore, a modification of the steel stress-strain relationship by Menegotto-Pinto [42] is proposed here to account for the degree of concrete damage surrounding the bar elements during the nonlinear cyclic analysis. The loss of bond between bars and surrounding cracked concrete is accounted for indirectly by reducing the stiffness contribution of the bars [36], which in turn is expected to contribute to the pinching effects. Thus, the use of a bond-slip model that would require defining new material parameters and an additional dof at each bar, is avoided.

Based on the proposed formulation presented in [36], the average of all reduction parameters a , expressed by Eq. 23, at the 8 GPs of any concrete hexahedral element, can be used to determine the level of damage D_s of the concrete material using Eq. 27.

$$D_s = [1 - a_{Element}] \quad (27)$$

$$a_{Element} = \frac{1}{n_{cr}} \sum_{i=1}^{n_{cr}} a_i, \quad (28)$$

where n_{cr} is the number of cracked GPs.

During unloading, when the structure reaches its initial deformation, the material deterioration of the bars can be calculated as:

$$E_s' = (1 - D_s) E_s \quad (29)$$

The material deterioration is applied when the criterion $\sigma_s \cdot \varepsilon_s < 0$ is satisfied, which describes the situations when crack closing and re-opening occurs, where the pinching phenomena are higher. In addition to the proposed modification in [36] and in order to capture pinching effects at the material level, the implementation of a reduced parameter R of the Menegotto-Pinto [42] model is proposed here:

$$R = R_0 - \frac{a_1 \xi}{\alpha_2 + \xi} \quad (30)$$

The values R_0 , a_1 and a_2 are determined by extensive numerical tests performed in [36] and are assumed to be 20, 18.5 and 0.15, respectively. By using the same concept described above and as presented in [36], the reduction factor D_R is proposed herein in order to decrease the parameter R into R' which is calculated as:

$$R' = (1 - D_R)R, \text{ where } D_R = D_s \quad (31)$$

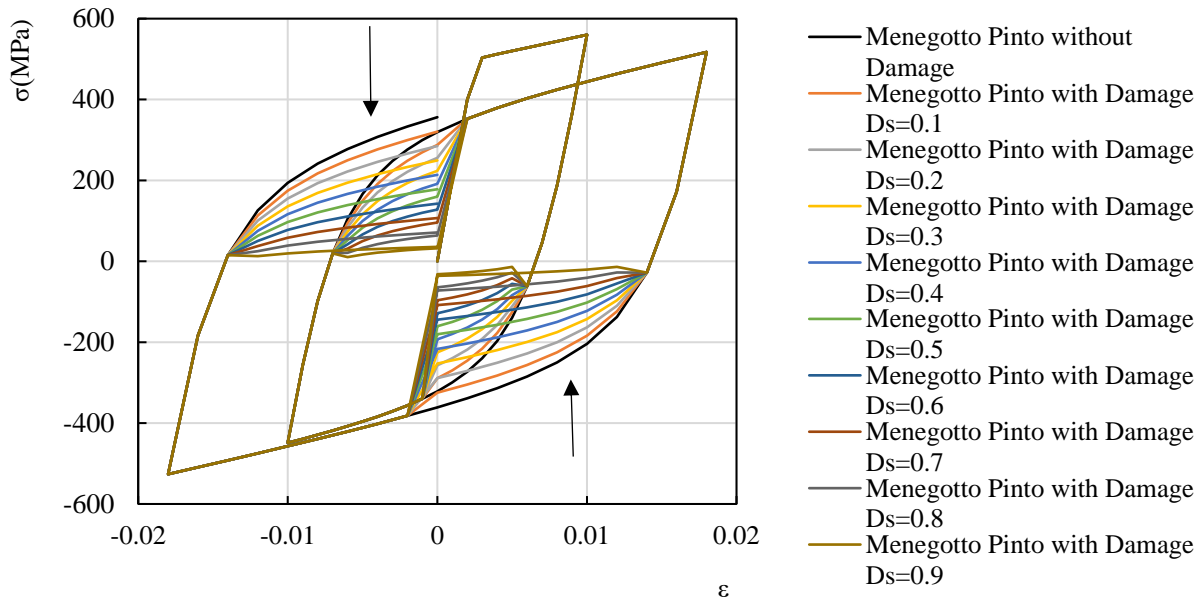


Figure 3: Modified Menegotto-Pinto steel model with parameters E' (Eq. 13) for different values of the damage factor

D_s .

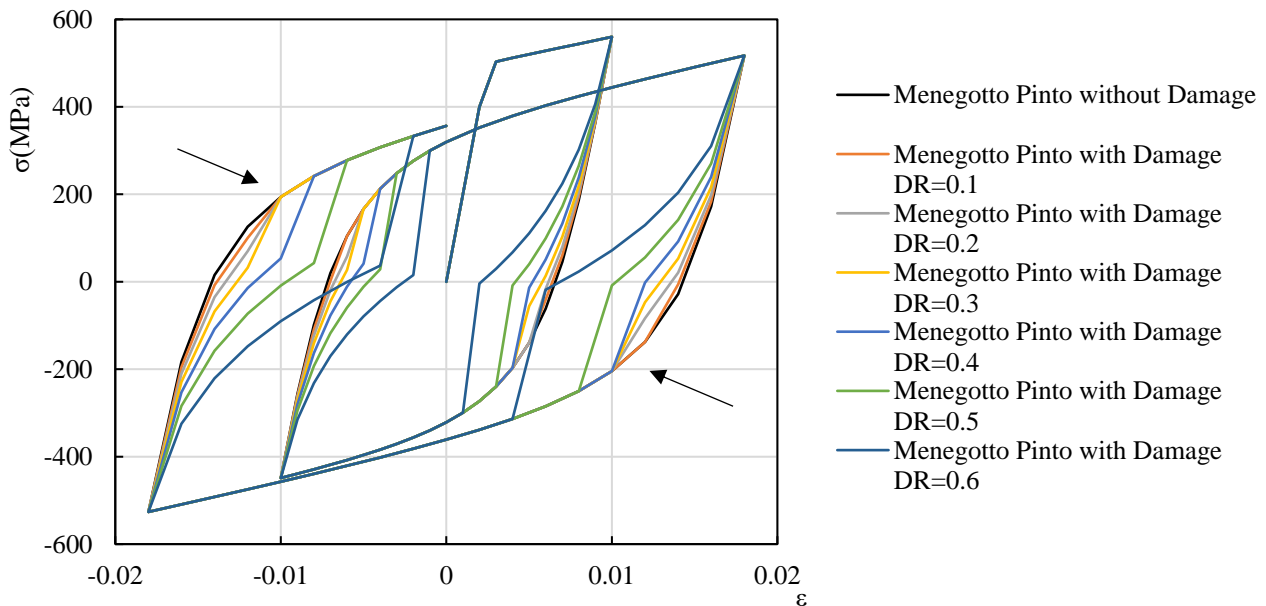


Figure 4: Modified Menegotto-Pinto steel model with parameter R' (Eq. 15) due to the opening and closure of cracks for different values of the damage factor D_R .

Fig. 3 shows the modified σ - ε curves of the Menegotto-Pinto material model with different steel damage factor D_S levels as proposed in [36], while Fig. 4 shows the modification of the σ - ε curves of the Menegotto-Pinto material model with the new steel damage factor D_R proposed in this study for different damage levels of concrete. Fig. 4 shows that the damage factor D_R modifies the stress-strain curves of the steel model in a similar manner to the D_S damage factor for concrete. However, in the case of D_R , the hysteretic loops of the material model tend to inflict a higher energy decrease as the accumulated damage in the surrounding concrete increases. This modified Menegotto-Pinto steel material model was found through preliminary parametric studies to be capable of capturing nonlinearities manifested by bar slip and significant energy losses within regions of excessively cracked concrete found around steel bars.

The modified σ - ε curves of the Menegotto-Pinto material model with both steel damage factors (D_S and D_R) are shown in Fig. 5 for different levels of concrete damage.

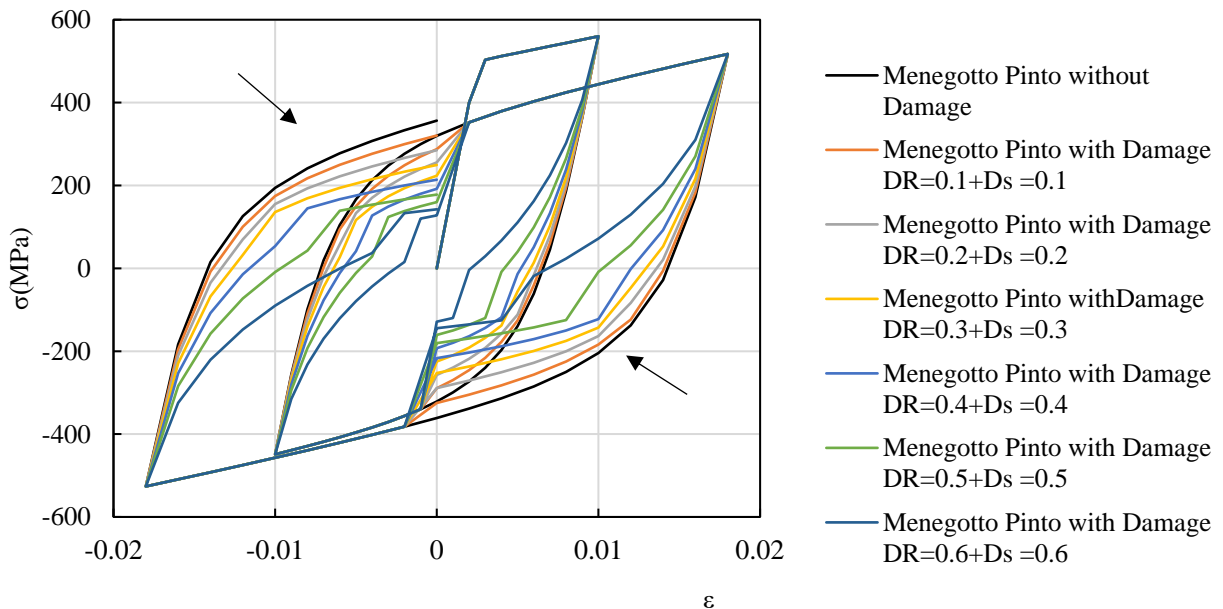


Figure 5: Modified Menegotto-Pinto steel model with parameters E' (Eq.13) and R' (Eq. 15) for different values of the damage factor D_R and D_S .

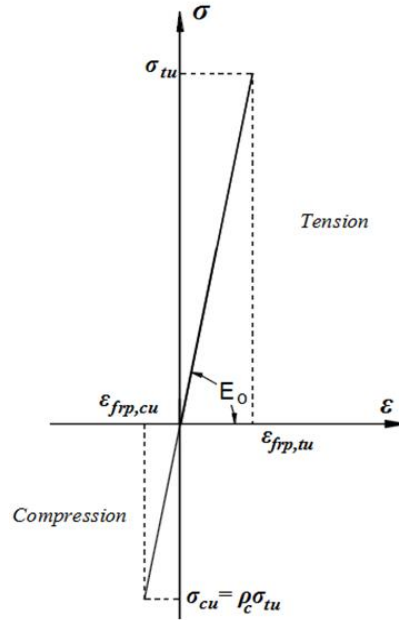


Figure 6: Material model of the CFRP jacketing [43].

The modified Menegotto-Pinto material model of Fig. 5 accounts for bar slip and other nonlinear phenomena that occur within the excessively cracked concrete regions. This is expected to capture different damage levels based on the cracks that occur at each GP within the concrete hexahedral elements. Indeed, the new damage factor D_R affects the hysteretic loops so that the higher the damage is within the concrete domain, the more the steel mechanical response is affected through a decrease in energy absorption, thus leading to smaller hysteretic loops. This also affects the corresponding internal force transferred from the bar to the concrete domain, simulating in this way the mechanism that occurs when slip initiates within a heavily cracked concrete region due to the loss of bond.

The stress-strain relationship of the CFRP jacketing is linear until failure occurs in both tension and compression (Fig. 6). As it can be seen, loss of capacity was assumed to occur when the ultimate stress at any GP of the CFRP hexahedral elements was reached. According to the reported material properties [36], the ultimate CFRP tensile strength was 4,140 MPa and the elastic modulus for both tension and compression was 241 GPa. It was also assumed that the CFRP 8-noded hexahedral elements used to discretize the jacketing were fully bonded to the concrete finite elements.

3. Experimental Data

The proposed modelling approach presented in section 2 is validated using experimental results

from three full-scale cyclic tests on deficient bare and CFRP-retrofitted RC joints tested previously by the authors [39]. The specimens simulated a 2D exterior joint between contra-flexure points of a floor in a multi-storey moment-resisting frame, but excluding the slabs (see Figure 7a). Figure 7b shows the cross sections and longitudinal reinforcement of column and beam. The longitudinal column bars were lapped for a length of 400 mm just above the joint core to represent typical deficient construction practices. Two types of anchorage detailing (types A and B) were examined, as shown in Figure 7c. The short straight anchorages of the beam are insufficient to develop the full capacity of the 16 mm bars. The column-to-beam flexural strength ratio ($\sum MR_{col} / \sum MR_{beam}$) was approximately 1.0, and therefore the strong column-weak beam strength hierarchy was not satisfied. Accordingly, the specimens were expected to fail at the joint core where no confining stirrups were provided. The column and beam were reinforced with 8 mm stirrups spaced at 150 mm centres to prevent a shear failure outside the joint core.

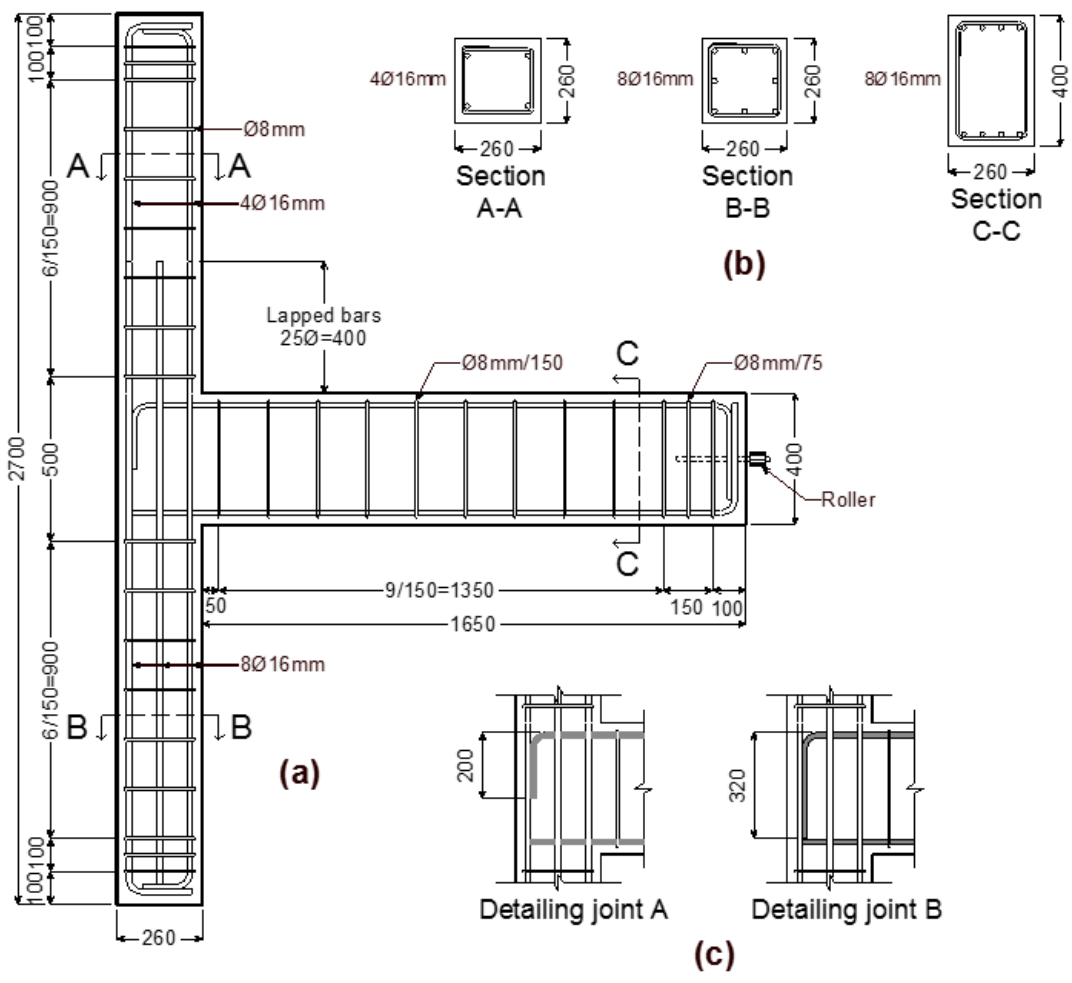


Figure 7: General geometry and reinforcement details of tested joints (units: mm) [39].

Table 1 shows the ID code of the specimens, as well as the concrete strength (f_{cm}), tensile concrete strength (f_{ctm}) and test condition [39]. The first letter of the ID stands for “Joint”, and the second for the type of detailing (A or B). Joints JA2 and JB2 were initially tested in bare conditions to produce severe damage to the core, according to the test setup shown in Figure 8, where the column is shown laying horizontally. The cyclic load was applied to the beam in displacement control using a servo-hydraulic actuator. Three push-pull cycles were applied at drift ratios δ (δ = beam tip displacement/beam length) ranging from $\pm 0.25\%$ and up to $\pm 5.0\%$. After the initial tests on joint JB2, the damaged concrete in the core was completely removed and replaced with new highly flowable concrete. Following the core replacement, the joint was retrofitted with externally bonded CFRP sheets, and the specimen was renamed JB2RF. The main goal of the CFRP retrofitting intervention was to i) prevent premature failure of the core zone, and ii) enhance the flexural capacity of the column. The failure of specimen JB2RF was dominated by the rupture of the CFRP sheets at drift ratios $\delta = \pm 5.0\%$. Figure 9 shows the final failure of specimens JB2 and JB2RF, where Fig. 10 shows the retrofitted specimen setup. The specimens were heavily instrumented with Linear Variable Differential Transformers (LVDTs) and linear potentiometers to measure displacement at the locations shown in Figure 8. Likewise, the strains in the reinforcement and CFRP strains were monitored by using foil-type strain gauges. Full details of the testing programme, instrumentation, retrofitting strategy and experimental results can be found in [39].

Table 1 Characteristics of beam-column joints.

ID	f_{cm} (MPa)	f_{ctm} (MPa)	Test conditions
JA2	32.0	2.44	Original bare joint, detailing A
JB2	31.3	2.41	Original bare joint, detailing B
JB2RF	55.3	3.67	JB2 retested with new recast core and CFRP retrofit

*Note: All values refer to the unconfined strength of concrete in compression and tension.

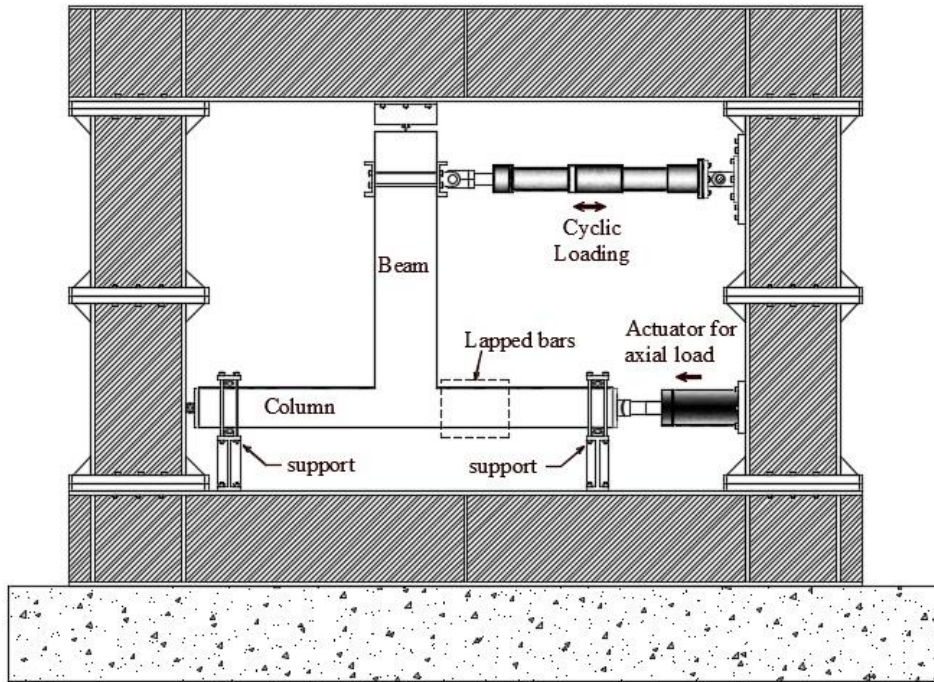


Figure 8: Test setup (units: mm) and instrumentation of RC joints, adapted from [39].

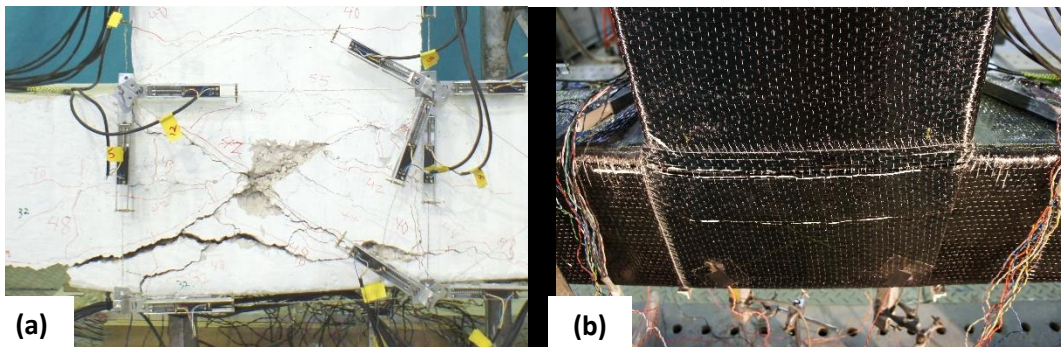


Figure 9: View of final failure mode of (a) bare joints (JB2), and (b) retrofitted joint JB2RF [39].

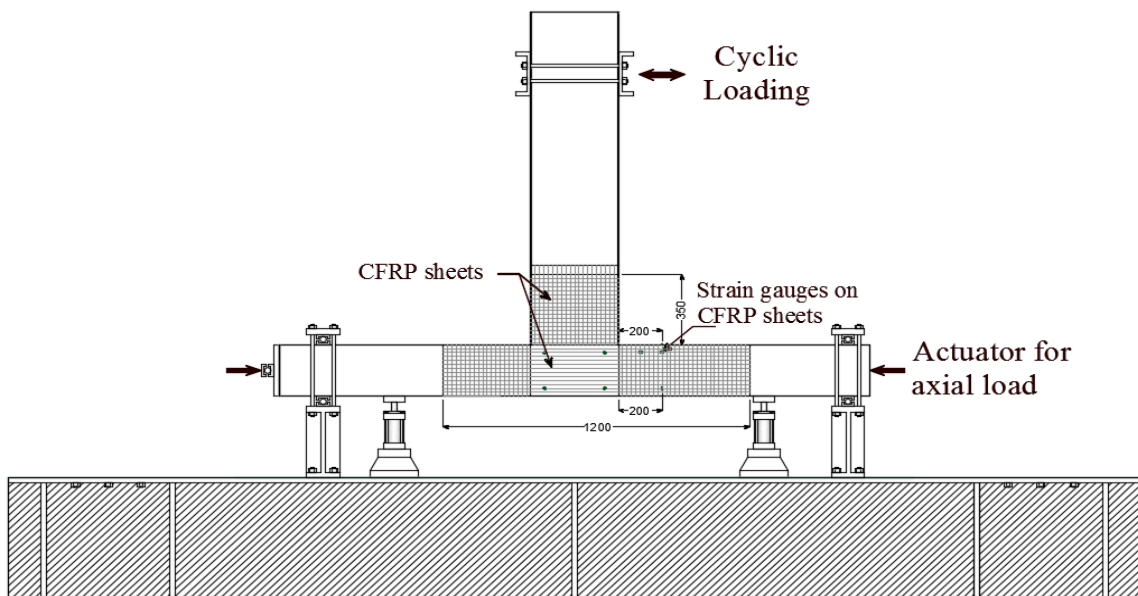


Figure 10: Test setup (units: mm) and instrumentation of retrofitted RC joints, adapted from [39].

4. Numerical Modeling, Results and Discussion

A numerical investigation was performed using the finite element models described in this section. A displacement control algorithm was implemented for all nonlinear analyses with the energy convergence criterion as expressed in Eq. 32. The energy convergence tolerance was set equal to 10^{-5} , which is in line with the numerical implementations presented in [2, 36-38, 44].

$$e_{err} = \frac{\Delta u_s^j \left\| F_s^{t+\Delta t} - R_s^{t+\Delta t} \right\|}{\Delta u_s^i \left\| F_s^{t+\Delta t} - R_s^t \right\|} \leq tolerance \quad (32)$$

4.1 Finite Element Mesh

Two finite element (FE) meshes were developed for specimens JA2, JB2 and JB2RF to investigate the numerical response of the proposed modelling approach. To study the mechanical behaviour of JA2 and JB2, the concrete domain was discretized with 8-noded hexahedral isoparametric finite elements and the steel reinforcement was discretized with Natural Beam-Column Flexibility-Based elements [37]. A total of 174 concrete and 500 steel elements were used to discretize the RC joint. 18 hexahedral 8-noded isoparametric steel finite elements (red colour) were used at the areas of the boundary conditions in order to prevent local failure (see Fig. 11). For the retrofitted RC joint (JB2RF), 156 additional hexahedral elements were used to discretize the CFRP jacketing that was assumed as fully bonded to the concrete elements (Fig. 12). The FE mesh and material details for the RC joints are given in Tables 2 and 3, respectively.

It must be noted that specimen JB2 was initially tested until failure, and subsequently rehabilitated with high strength concrete (HSC) and retrofitted with CFRP sheets. The normal strength and HSC domains were discretized and modelled accordingly based on the experiments performed in [36]. Fig. 11 shows the concrete elements used in the modelling: 1) red colour represents the steel hexahedral elements, 2) grey coloured elements correspond to standard concrete, and 3) the white elements represent the HSC domain. All concrete hexahedral elements of JA2 and JB2 (bare RC specimens) were assigned normal concrete material properties, while the concrete hexahedral elements found in the core of JB2RF (shown in white colour) were assigned HSC material properties based on the data

provided in Table 3. Before moving to the next section, where the numerical investigation's results will be presented, it is noteworthy to say at this point that the proposed modeling approach was implemented through the research software Reconan FEA [45].

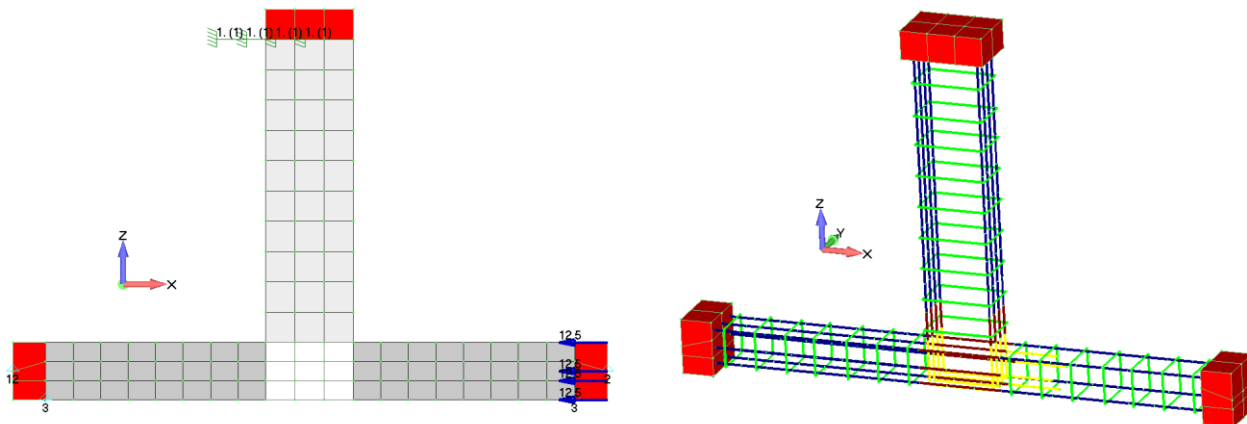


Figure 11: Bare RC joints JA2 and JB2. (Left) Hexahedral and (Right) embedded rebar finite elements.

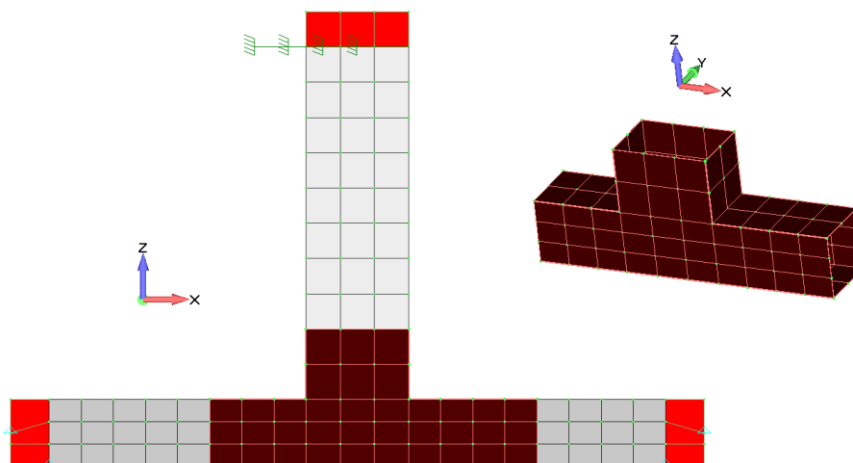


Figure 12: Retrofitted RC joint JB2RF. Concrete and CFRP hexahedral finite element meshes.

Table 2 FE mesh details of the RC Joint models.

a/a	Model	Total Number of Nodes	Hexahedral Elements	Embedded Rebar Elements
1	JA2/JB2	396	192	500
2	JB2RF	620	348	500

Table 3 Material details used in the FE model.

Material	Young Modulus (GPa)	Hardening Modulus (GPa)	Yielding Stress / Tensile Strength* (MPa)	Compressive Strength (MPa)	Shear remaining strength β	Poisson Ratio	Ultimate Strain ε
Concrete	20	-	2.41*	31.3	0.03	0.2	-
High Strength Concrete	30	-	3.91*	55.3	0.05	0.2	-
Steel Rebars	190	1	551 (Ø16) / 612 (Ø8)	-	-	0.3	15%
CFRP	241	-	4,140*	-	-	0.3	1.7%

4.2 Numerical Results for Bare Joints

The first set of imposed cyclic loading applied cycles with up to 3% deformation for the case of the JA2 model. Fig. 13 compares the numerical results and the experimental data and shows that the proposed modelling approach reproduces well the test results of the bare RC joint. The extreme pinching observed in the test was also successfully numerically reproduced, indicating that the proposed material damage factors for steel and concrete can capture both material deterioration and bar slippage.

The main differences between the experimental and numerical curves can be attributed to the displacement history that was imposed in a static manner in the cyclic nonlinear analysis, while the experimentally imposed horizontal displacements were not kept constant (due to creep) at each set of cycles, as shown in the experimental curve given in Fig. 13. Therefore, the numerical analysis produced curves with constant horizontal displacements at each set of three cycles. However, the strength deterioration of the numerical model can be clearly observed.

In Table 4, the comparisons between the numerical and experimental peak values for each cycle are presented. It can be seen, that between the first 13 Cycles, the numerical approach managed to capture the experimental peak load with an average divergence from the experimental data of 10%, thereafter the damage due to the excessive deformation increased significantly, where the divergence of the numerical results increased as well. However, after the 13 cycles, the experimental results show a significant decrease in strength of the RC joint. On the contrary, the numerical model presents the

same strength in the last cycles because of the absence of strain softening behaviour of concrete. The strain softening will cause a significant increase in the numerical cost and convergence issues under these extreme conditions. Therefore, the damage of concrete does not increase significantly, and the behaviour of the structure is mostly affected by the plastic behaviour of steel reinforcement.

A similar numerical response is noted in Table 5, where the comparison between the numerical and experimental results in terms of dissipated energy is shown. The differences depicted at the beginning of the experiment between the numerical and experimental data are higher, a phenomenon attributed to the inability of accounting the initial condition of the RC specimen, while the numerical model does not take into account any initial damage nor cracking found within the specimen prior to the initiation of the experiment. As the cyclic loading progresses, the dissipated energy is reproduced in a more accurate manner, where the last loading cycle is captured with an 11% error.

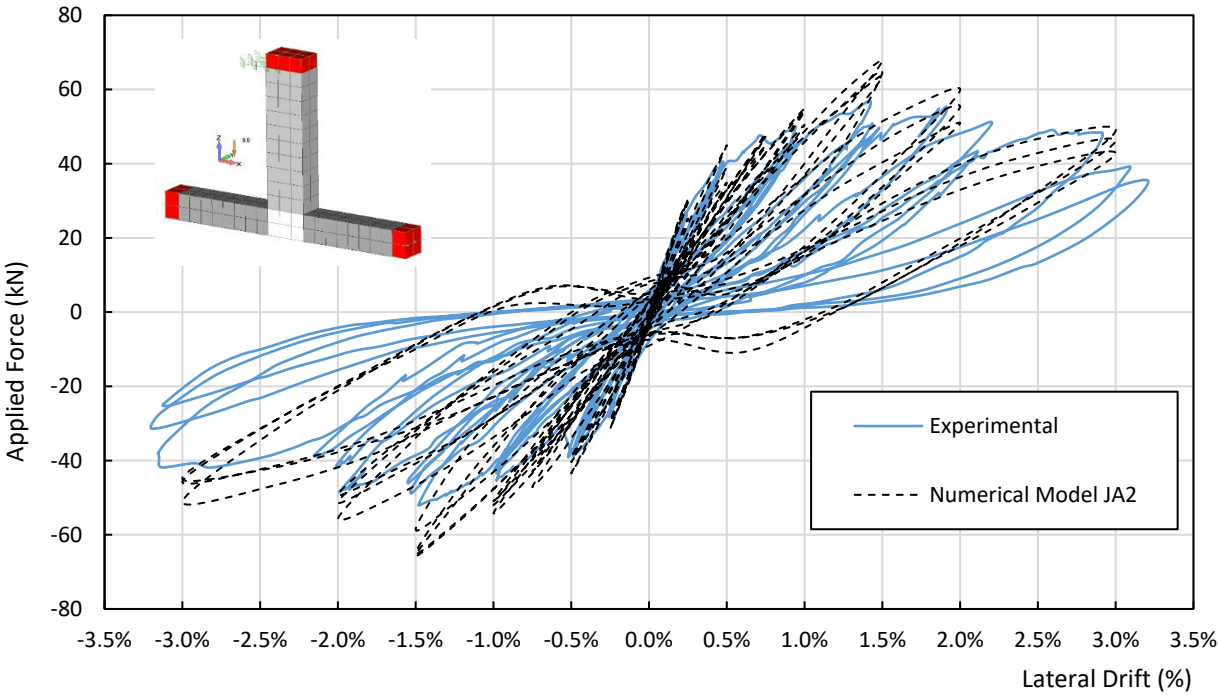


Figure 13: JA2 Joint. Comparison between the numerical and experimental load vs drift curves. Maximum horizontal deformation 50 mm.

Table 4 JA2. Comparison between numerical and experimental results in terms of the peak load developed in each cycle.

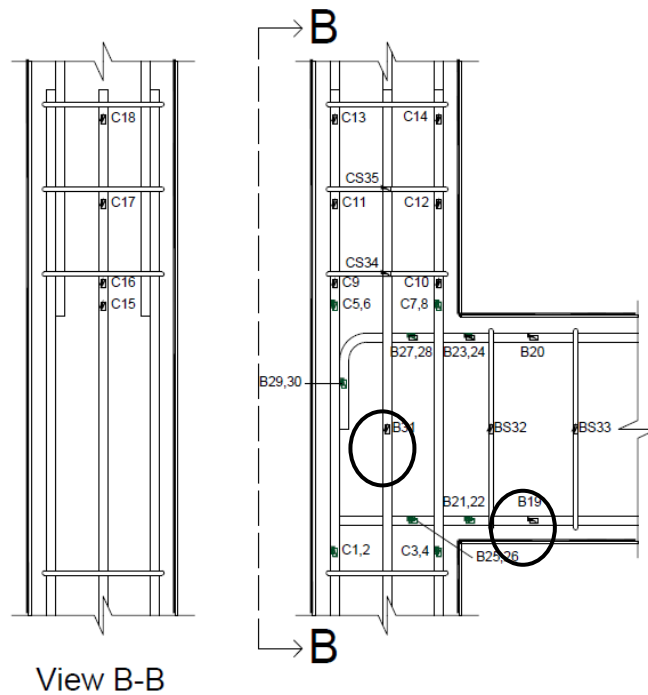
JA2	Peak Load (kN)		

	Experimental		Numerical		Divergence	Divergence
	(+)	(-)	(+)	(-)	(+)	(-)
Cycle 1	26.91	-28.23	30.51	-31.49	13.37	11.56
Cycle 2	26.82	-24.42	29.58	-29.46	10.30	20.61
Cycle 3	26.50	-24.94	25.21	-29.29	4.88	17.45
Cycle 4	40.60	-38.78	44.97	-43.47	10.78	12.09
Cycle 5	39.87	-37.86	38.93	-40.45	2.35	6.82
Cycle 6	39.96	-39.12	34.86	-39.09	12.77	0.08
Cycle 7	49.87	-45.43	48.13	-47.14	3.48	3.75
Cycle 8	46.25	-43.44	44.88	-42.95	2.97	1.12
Cycle 9	45.73	-42.59	47.27	-39.90	3.37	6.32
Cycle 10	56.98	-51.93	54.19	-54.21	4.88	4.40
Cycle 11	50.81	-48.84	54.74	-50.94	7.73	4.29
Cycle 12	49.70	-46.08	50.46	-51.88	1.53	12.58
Cycle 13	55.29	-48.45	67.73	-64.93	22.50	34.00
Cycle 14	50.67	-41.82	63.62	-65.62	25.55	56.89
Cycle 15	43.36	-38.90	64.78	-58.44	49.38	50.21
Cycle 16	49.11	-41.89	59.90	-55.80	21.97	33.21
Cycle 17	39.25	-31.39	55.45	-51.33	41.27	63.52
Cycle 18	35.22	-25.22	50.95	-49.09	44.65	94.63

Table 5 JA2. Comparison between numerical and experimental results in terms of the dissipated energy in each cycle.

JA2	Dissipating Energy (kN mm)		Divergence (exp-num)/exp (%)
	Experimental	Numerical	
Cycle 1	32.73	7.95	75.72

Cycle 2	15.39	51.26	233.17
Cycle 3	13.39	6.18	53.88
Cycle 4	87.39	15.30	82.49
Cycle 5	48.55	28.18	41.97
Cycle 6	48.19	17.91	62.84
Cycle 7	338.02	59.49	82.40
Cycle 8	158.10	54.84	65.31
Cycle 9	120.29	51.25	57.39
Cycle 10	451.09	111.66	75.25
Cycle 11	265.67	116.86	56.02
Cycle 12	160.86	118.86	26.11
Cycle 13	516.61	304.31	41.09
Cycle 14	461.96	302.00	34.63
Cycle 15	302.19	481.97	59.50
Cycle 16	1213.03	764.46	36.98
Cycle 17	738.82	564.91	23.54
Cycle 18	557.86	495.60	11.16



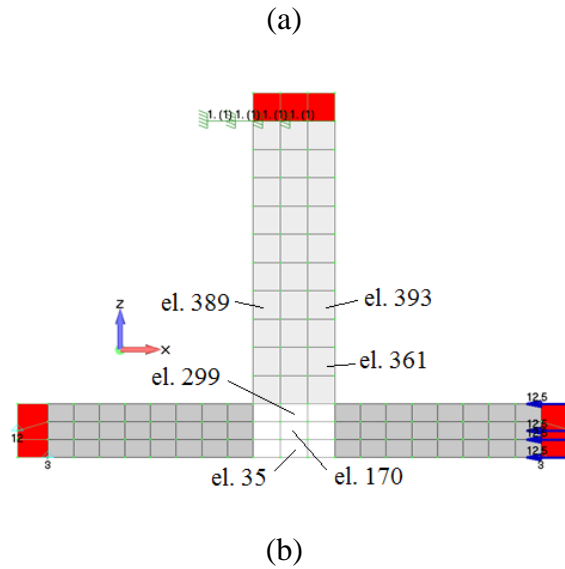


Figure 14: JA2 Joint. (a) Gauge locations [39] and (b) hexahedral element IDs and locations on the FE mesh.

One of the greatest challenges in computational mechanics is to develop a numerical model that captures the overall mechanical behaviour of RC specimens but at the same time to be able to reproduce experimental measurements at the material level. The most representative physical measure that has its own practical challenges, is the measure of strains at the rebar level. To further compare the numerical and experimental results, the experimentally measured bar strains at two different locations (gauges B19 and B31) within the joint are examined. Fig. 14a shows the gauges that were installed in JA2 on the steel rebars and the corresponding hexahedral elements that were monitored to determine strains (Fig. 14b). It must be noted that the assumption of full bond between the bar and hexahedral concrete finite elements (FEs) implies that the deformation of the two elements is the same. However, the deformation of the steel rebars is expected to be larger than the actual physical deformation according to this numerical assumption, mainly because the damage factors will cause larger deformations on the steel rebar based on the modified material response.

Fig. 15 compares the numerically predicted strain history and experimental readings of gauge B19 (see Fig. 15b; ZZ-strain of FE 361). As expected, the predicted strain is higher, which confirms that the damage factors that introduce the material deterioration at the rebar level control this numerical phenomenon. Figs 15c and 15d show the ZZ-strain of hexahedral elements 393 and 389, respectively. In this case, the numerically computed curves are smaller and closer to the experimental data, given

that they are located in areas which are not excessively cracked. Therefore, they represent a mechanical behaviour of an RC volume with insignificant slippage.

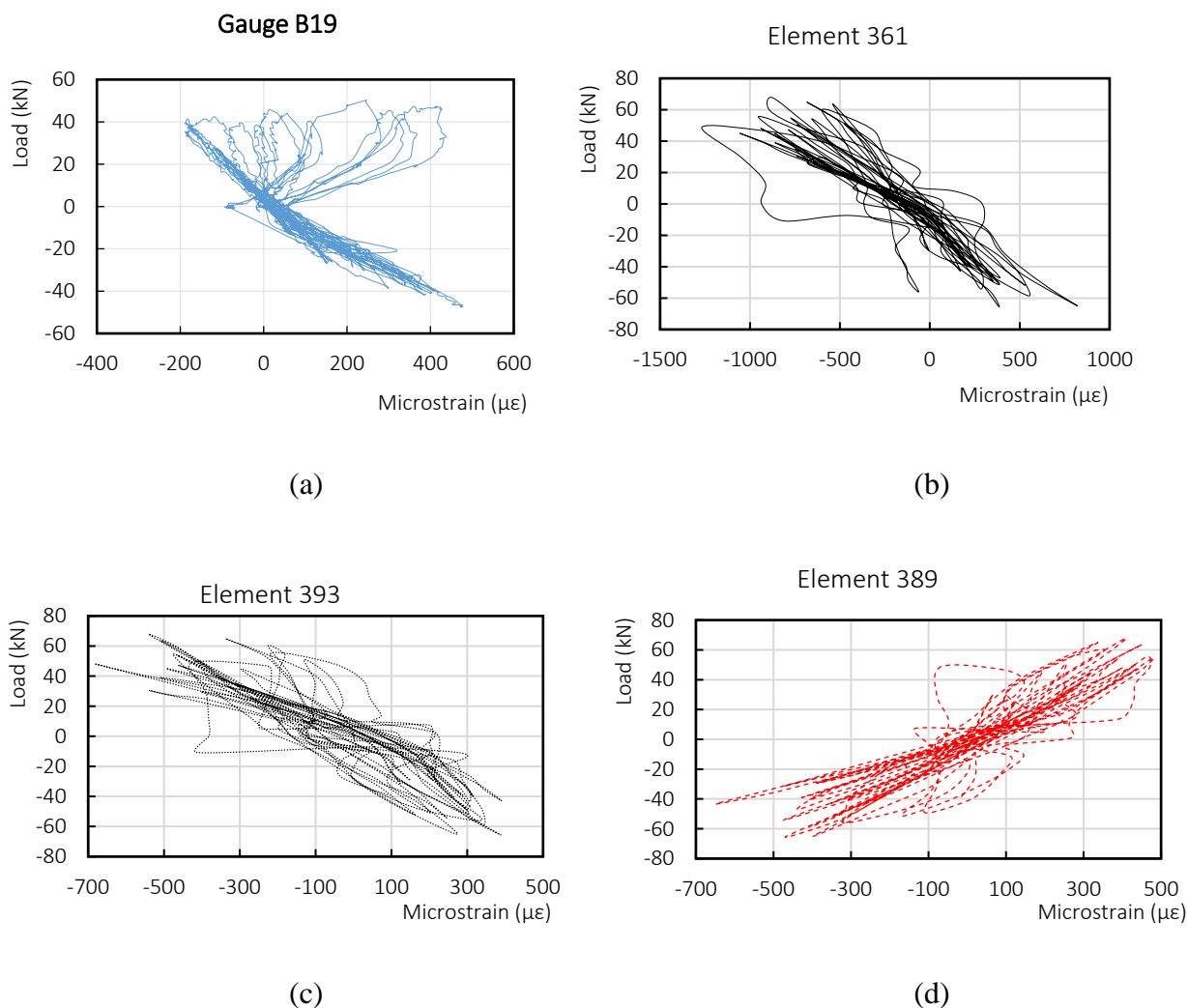


Figure 15: JA2 Joint. ZZ-strain histories of (a) experimental gauge B19, (b) element 361, (c) element 393 and (d) element 389.

Fig. 16 compares the XX-strain computed at hexahedral elements 35, 170 and 299 and the readings from gauge B31. Even though gauge B31 was located within an area that developed excessive cracking, the bar did not slip excessively. This observation is also reflected in the computed load-strain curves, as shown in Fig. 16. It is important to note that the strains in Fig. 16a highlight the complexity of the problem at hand, where the continuum problem of uncracked concrete is transformed into a concrete domain with significant discontinuities. Nonetheless, the proposed model that incorporates principles of continuum mechanics in combination with the smeared crack approach, manages to provide the proposed modelling method with the ability to avoid the use of a discrete modelling

method that would have induced significant instabilities and increased computational demand.

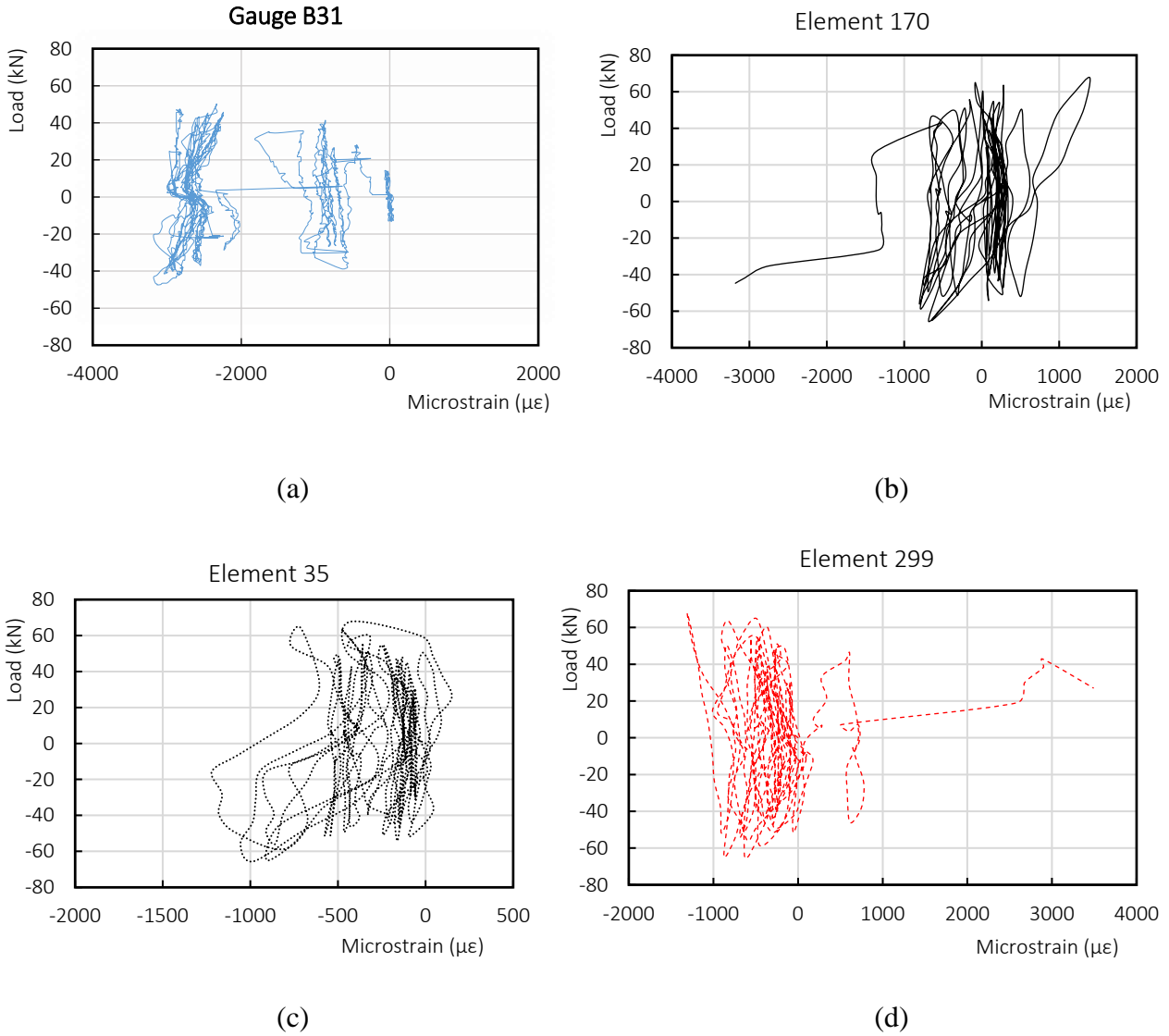


Figure 16: JA2 Joint. XX-strain histories of (a) experimental gauge B31, (b) element 170, (c) element 35 and (d) element 299.

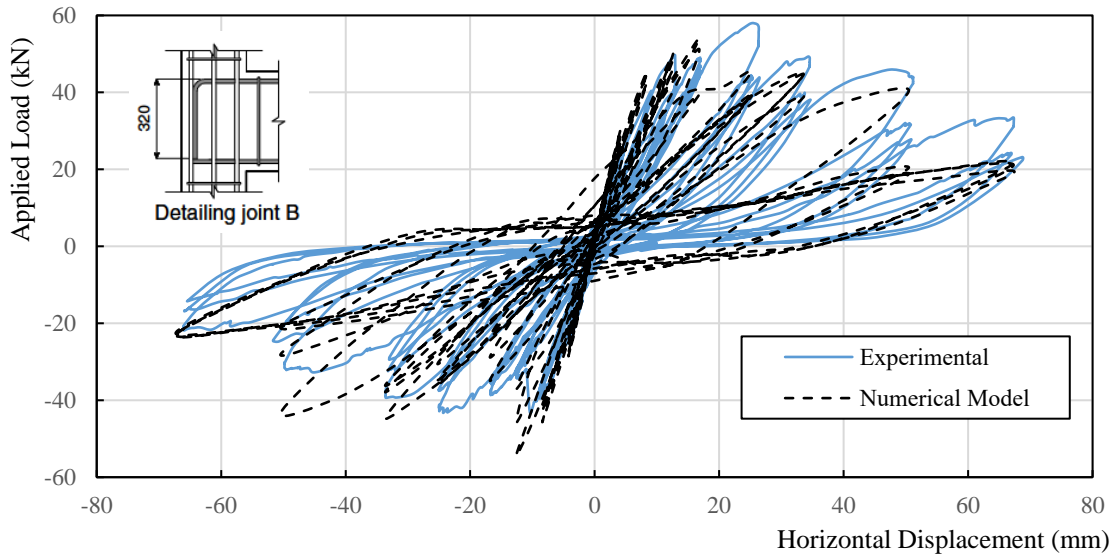


Figure 17: JB2 Joint. Comparison between the numerical and experimental P- δ curves.

Fig. 17 compares the experimental and numerical results of joint JB2. It is shown that, in general, the modelling approach captures well the strength deterioration observed in the experiment. The experimental data show a strength drop larger than 50%, also found in the numerical analysis. Especially in cases where the imposed horizontal displacements were larger than 50 mm, the reaction measured along the horizontal direction was found to decrease significantly. According to the experimental data, the maximum computed positive reaction was 58 kN, whilst during the last loading cycle it dropped to 21.8 kN (2.66 times smaller). The corresponding maximum numerically predicted reaction was 54.2 kN, where the respective final reaction during the last loading cycle was computed to be equal to 19.6 kN (2.76 times smaller). Based on these reactions, the numerical model managed to capture the maximum reaction with a 6.6% error, the final reaction during the last cycle with a 10% error, while the overall drop was predicted with a 3.8% error. It is worth mentioning that the extreme nonlinearities, observed in JA2 and JB2, developed during the last loading cycles of the tests were well captured by the proposed modelling method.

The above conclusions can be further supported by Table 6 where the comparison of the peak loads that are developed in each cycle for both numerical and experimental results, are compared. The average divergence for the positive and negative peak loads is 14.92 and 18.45%, respectively.

Table 6 JB2. Comparison between numerical and experimental results in terms of the peak load developed in each cycle.

JB2	Peak Load (kN)				Divergence (+)	Divergence (-)
	Experimental		Numerical			
	(+)	(-)	(+)	(-)		
Cycle 1	26.21	-25.65	30.67	-28.57	17.01	11.38
Cycle 2	24.77	-24.96	28.86	-27.62	16.52	10.64
Cycle 3	24.40	-23.96	27.04	-25.24	10.83	5.33
Cycle 4	40.41	-39.59	45.69	-45.69	13.08	15.41
Cycle 5	37.64	-40.34	45.47	-43.03	20.80	6.66
Cycle 6	38.84	-38.20	42.53	-41.17	9.50	7.78

Cycle 7	49.72	-43.10	50.09	-54.45	0.75	26.32
Cycle 8	42.21	-33.44	48.78	-45.64	15.58	36.47
Cycle 9	40.91	-32.45	45.94	-37.07	12.30	14.23
Cycle 10	49.05	-38.68	54.15	-34.89	10.40	9.79
Cycle 11	46.94	-35.98	51.05	-28.83	8.76	19.88
Cycle 12	45.45	-35.82	39.58	-23.34	12.90	34.84
Cycle 13	57.97	-43.27	45.55	-30.53	21.42	29.46
Cycle 14	44.44	-37.56	39.52	-36.01	11.07	4.12
Cycle 15	43.87	-34.66	39.12	-34.76	10.83	0.28
Cycle 16	49.31	-39.36	44.94	-44.65	8.86	13.44
Cycle 17	39.86	-32.45	44.73	-36.18	12.21	11.48
Cycle 18	37.98	-29.46	39.00	-37.89	2.68	28.61
Cycle 19	45.91	-32.77	40.49	-43.49	11.82	32.73
Cycle 20	32.03	-24.72	20.50	-28.21	35.99	14.13
Cycle 21	27.81	-19.55	18.82	-21.19	32.34	8.36
Cycle 22	33.48	-21.86	21.14	-23.13	36.87	5.79
Cycle 23	24.24	-16.88	21.79	-23.10	10.10	36.81
Cycle 24	23.18	-14.21	19.60	-22.58	15.46	58.97
Avg					14.92	18.45

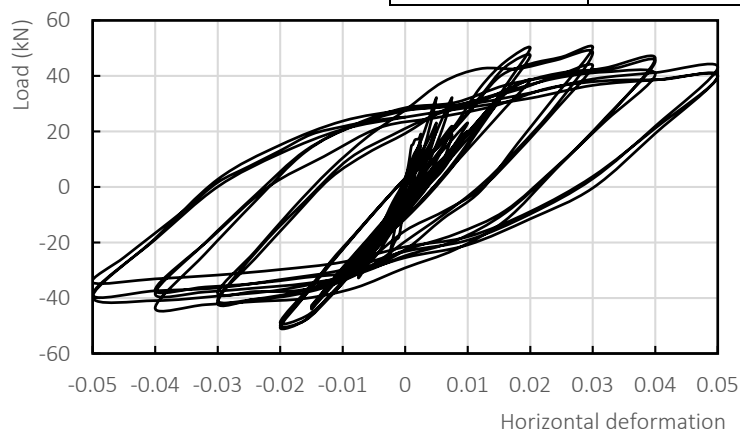


Figure 18: JB2 Joint. P- δ curve when not using the proposed steel damage factor in Eq. 31.

Before presenting the results derived from the next specimen, the numerically obtained hysteretic loops are shown in Fig. 18, where the newly proposed damage factor of Eq. 31 is not activated. As it

can be seen, the numerically derived curve fails to capture the overall mechanical response of the specimen given that the pinching effect is not visible in this case, over-estimating the dissipated energy significantly (see Table 7). It is easy to see the significant differences given in Table 7 in terms of energy dissipation between the numerical models when activating and deactivating the proposed damage factors, where the average difference is found to be equal to 206%. This shows in a quantitative manner the ability of the proposed model to capture the pinching effect. Furthermore, the analysis that foresees the use of concrete and steel materials without the damage factors fails to at loading cycle 23, due to numerical divergence. A similar response was recorded for the rest of the models presented in this manuscript, thus for brevity reasons they will not be shown.

Table 7 JB2. Comparison between numerical with and without damage factors in terms of the dissipated energy in each cycle.

JB2	Dissipating Energy (kN mm)		Divergence
	With Damage Factors	Without Damage Factors	
Cycle 1	8.45	53.19	530%
Cycle 2	8.5	49.92	487%
Cycle 3	7.87	118.70	1408%
Cycle 4	30.64	157.43	414%
Cycle 5	35.9	164.81	359%
Cycle 6	39.08	301.28	671%
Cycle 7	89.35	258.10	189%
Cycle 8	121.33	334.03	175%
Cycle 9	78.63	364.86	364%
Cycle 10	132.98	440.41	231%
Cycle 11	243.45	780.19	220%
Cycle 12	141.17	788.15	458%
Cycle 13	422.73	1175.78	178%
Cycle 14	151.44	1363.84	801%

Cycle 15	192.8	1787.36	827%
Cycle 16	470.86	1638.84	248%
Cycle 17	429.69	1965.89	358%
Cycle 18	233.53	2337.91	901%
Cycle 19	1219.39	2332.50	91%
Cycle 20	905.91	2399.30	165%
Cycle 21	1020.42	2889.03	183%
Cycle 22	1615.53	1580.09	2%
Cycle 23	1442.53	-	-
Cycle 24	1498.79	-	-
Avg	345.44	1058.26	206%

4.3 Analysis Results of the Retrofitted Joint

As previously described, after the completion of the JB2 test, the severely damaged substructure was rehabilitated with HSC and retrofitted with CFRP sheets. After retrofitting the damaged specimen, it was renamed into JB2FR and the FE model that was presented in section 4.1 (see Fig. 12) was used to simulate its mechanical response. According to [39], the retrofitted joint was once more subjected to extreme cyclic loading until complete failure. The main goals of the rehabilitation and retrofitting were to double the capacity of the joint, and to achieve a weak-beam strong-column behaviour [39].

Fig. 19 compares the experimental and numerical P- δ curves of JB2FR. The results show that the extreme pinching observed in the experiments were captured well. The maximum experimentally measured positive reaction was 122.5 kN, while the corresponding numerical value was 114.1 kN for a total of 40 mm horizontal displacement. The negative maximum reaction was 125.3 kN, whereas the measured value was 125.8 kN for a negative 40 mm horizontal displacement. These results confirm the ability of the proposed modelling method to reproduce experimental results of retrofitted substructures that undergo ultimate limit state cyclic loading. This also further validates the ability of the developed algorithm presented in [2, 36, 43] to capture the mechanical response of CFRP

retrofitted RC structures.

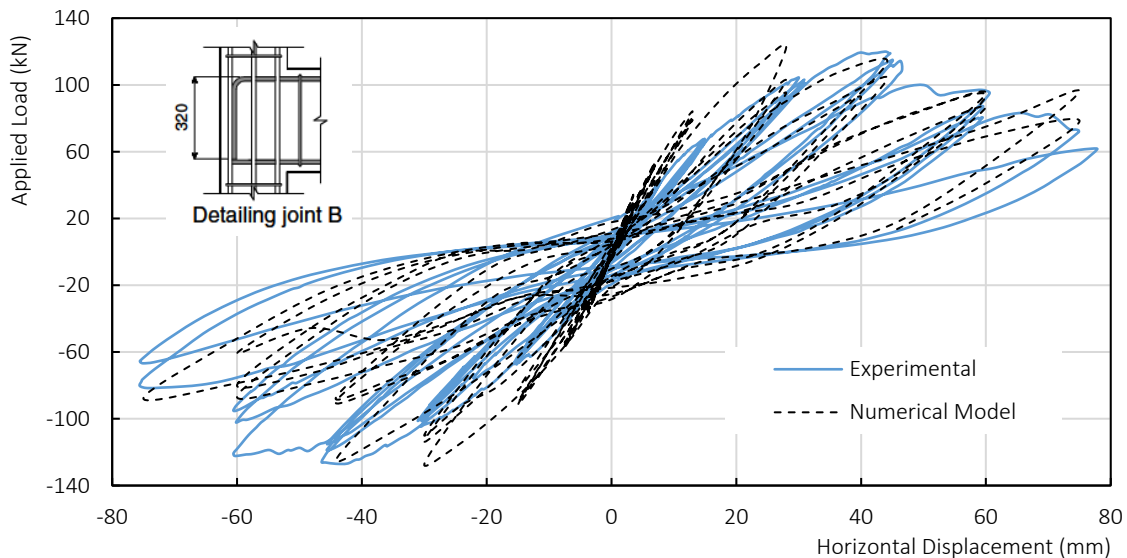


Figure 19: JB2FR Joint. Comparison between the numerical and experimental results.

Based on the numerically obtained curve in Fig. 19, it is worth mentioning that the numerical model had a stiffer behaviour during the initial cycles (less than 25 mm). This numerical phenomenon can be attributed to the initial concrete damage produced on JB2, which was not accounted for during the numerical analysis of JB2FR. However, this numerical phenomenon was not significant at larger displacements. The challenges of representing the exact geometry and the material properties of a damaged/retrofitted specimen are significant and the level of uncertainty is relatively high. Nonetheless, it is evident that the proposed modelling method can capture the full P- δ curve of the joint at a very acceptable level.

Table 8 shows the comparison between the numerical and the experimental results in terms of the peak load presented in each cycle. During the initial cycles, the numerical model seems to overestimate the strength of the structural member. After the 5th cycle, the developed damage of the numerical model captures the experimental results with accuracy that starts with 25% and reaches values with divergence below 5%. This is attributed to the initial state of the numerical model that does not account the specimen's strength deterioration prior to testing. The JB2RF specimen was rehabilitated and strengthened, but the column and beam did develop cracks that were not visible to the naked eye, or they were found within the concrete domain. Therefore, this initial damaged state was not able to be

accounted for and therefore the numerical results derived this divergence at the initial stage of the analysis. Conclusively, this extremely complicated problem and the corresponding obtained numerical results, further demonstrate the abilities of the proposed modeling method in capturing the overall mechanical response of this type of structures under ultimate limit state cyclic loading conditions.

Table 8 JB2RF. Comparison between numerical and experimental results in terms of the peak load developed in each cycle.

JB2RF	Peak Load (kN)				Divergence (+)	Divergence (-)
	Experimental		Numerical			
	(+)	(-)	(+)	(-)		
Cycle 1	23.26	-28.49	34.25	-35.54	47.25	24.74
Cycle 2	23.37	-24.68	33.47	-35.98	43.21	45.82
Cycle 3	21.98	-24.07	30.36	-35.63	38.14	48.02
Cycle 4	42.66	-44.10	53.99	-57.41	26.58	30.19
Cycle 5	42.24	-42.32	51.90	-54.29	22.87	28.30
Cycle 6	42.04	-42.83	52.92	-55.61	25.88	29.85
Cycle 7	67.70	-67.47	80.96	-91.73	19.59	35.96
Cycle 8	66.59	-66.68	84.15	-89.96	26.36	34.91
Cycle 9	65.78	-66.34	78.98	-82.72	20.06	24.69
Cycle 10	104.52	-104.50	122.52	-127.62	17.22	22.12
Cycle 11	102.91	-101.33	102.82	-109.95	0.09	8.51
Cycle 12	101.05	-101.04	95.27	-113.35	5.72	12.18
Cycle 13	119.98	-126.95	114.13	-125.29	4.87	1.31
Cycle 14	115.04	-118.88	104.21	-87.94	9.41	26.03
Cycle 15	114.33	-115.26	92.77	-90.05	18.86	21.88
Cycle 16	99.64	-122.20	93.39	-80.11	6.27	34.44
Cycle 17	87.33	-102.10	95.33	-86.92	9.16	14.86
Cycle 18	80.56	-95.15	86.97	-60.76	7.95	36.15
Cycle 19	83.20	-81.59	96.19	-87.82	15.62	7.63

Furthermore, the numerical model managed to capture the drop in-terms of strength with a 9% deviation compared to the experimental curve for the negative horizontal displacement, while the corresponding final positive reactions were computed with a 15% and a 25% error for the last two maximum imposed positive horizontal displacements. This numerical finding is attributed to the initial stiffer behaviour of the numerical model that did not account for the cracked areas of the column and beam members that were developed during the first cyclic test that caused JB2 to fail. Additionally, the full-bond assumption between the CFRP sheets and the concrete surface contributed to this numerical phenomenon as well.

The ability of the proposed model to capture the strains on the CFRP sheets of JB2FR is also studied using the test results. Readings from strain gauges located at the core zone indicated that CFRP strains were close to zero at the initial stages of loading, however, these increased after diagonal cracks developed at the core [39]. Fig. 20 shows that the numerical results match well the experimental data. According to [39], the CFRP strain at peak load was 7,300 $\mu\epsilon$, while the corresponding numerically predicted value was equal to 6,250 $\mu\epsilon$ (see Fig. 20). Finally, the strain for the ultimate horizontal displacement reported in [39] was equal to 16,900 $\mu\epsilon$, where the numerical prediction was 9,600 $\mu\epsilon$. These results indicate that the strain prediction for the peak load was realistic and with an acceptable accuracy of 14%, whereas the ultimate strain at maximum displacement was computed with a variation of 43%. This is attributed to the fact that the numerical model had a stiffer overall behaviour as described above (pre-existing cracks and yielded rebars were not accounted for thus lower strains were developed at the confined concrete volume), whereas the analysis finished half a cycle prior to the application of the last maximum displacement, where the ultimate strain was measured experimentally.

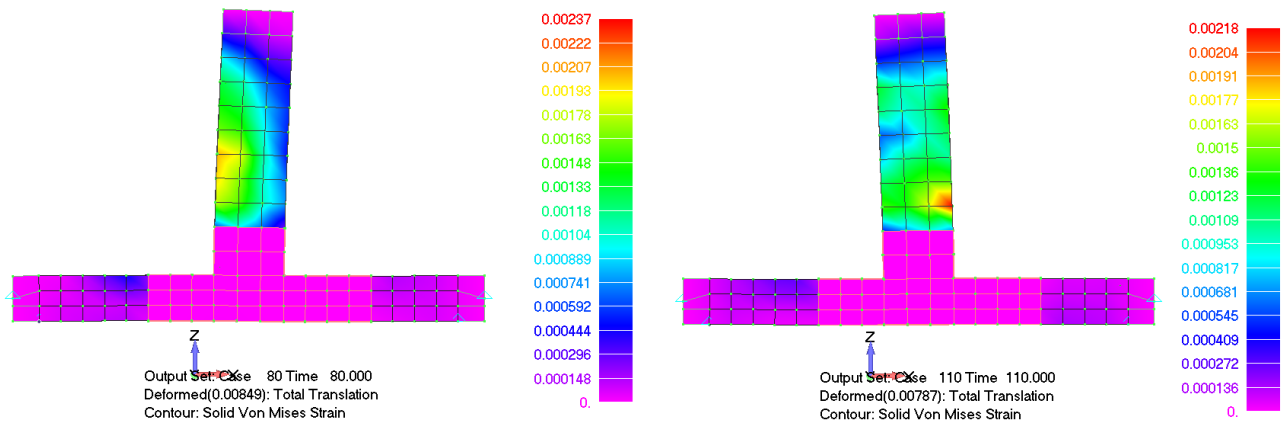


Figure 20: JB2FR Joint. Von Mises strain contour at horizontal displacement (a) 7.5 mm and (b) -7.5 mm.

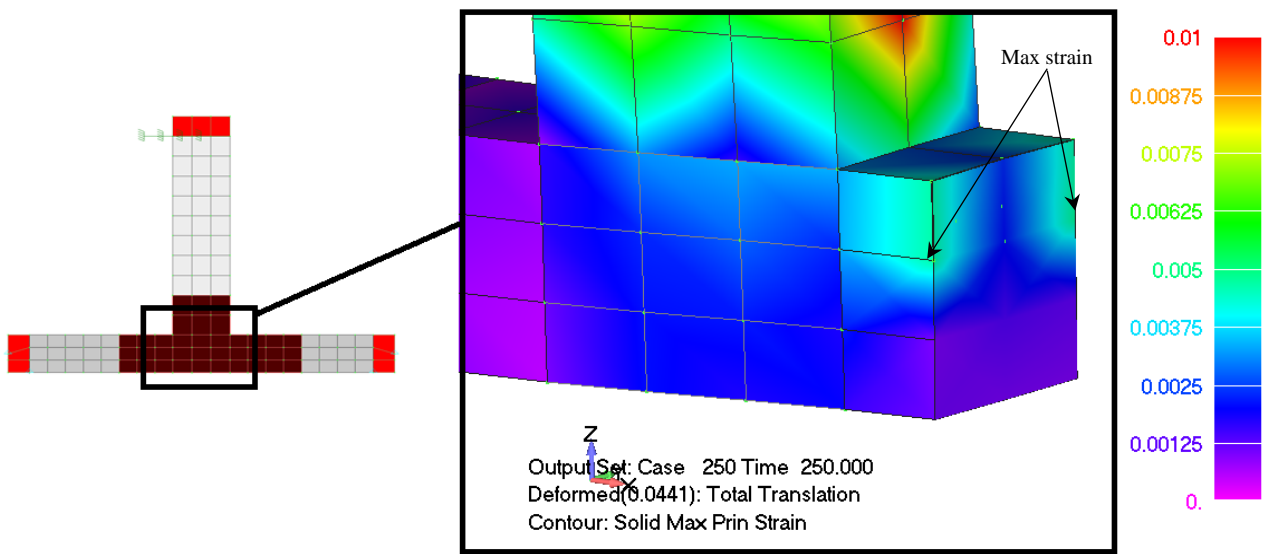


Figure 21: JB2FR Joint. Max principal strain contour at peak load ($\epsilon = 6250 \mu\epsilon$, $P_u = 114.13 \text{ kN}$).

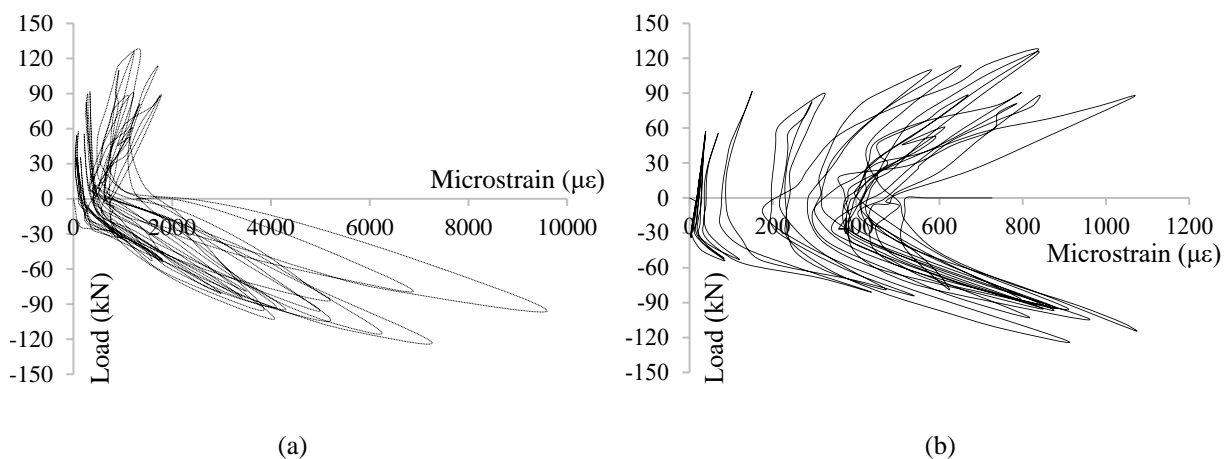


Figure 22: JB2FR Joint. CFRP strain vs load at the (a) core and (b) column lap splices. Numerical results.

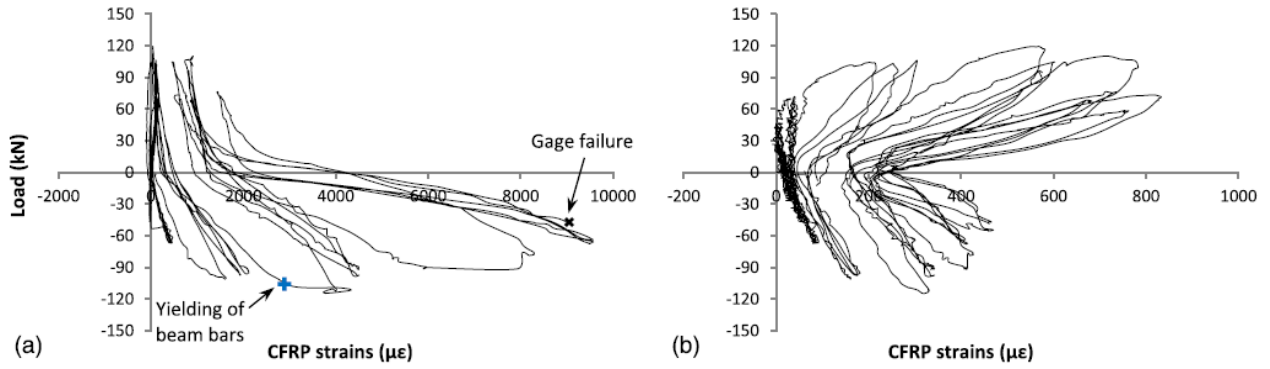


Figure 23: Strains recorded in CFRP sheets at (a) core; (b) column lap splices of joint JC2RF [39].

In order to further investigate the strain development at the CFRP sheets, Fig. 22 shows the maximum principal strain and the applied load. The finite element location on the CFRP sheet that was used to develop the graph of Fig. 22, is shown in Fig. 23 and coincides with the location of the gauge used on confining sheets 6 at the midpoint of the lap splice length (see Fig. 10). Based on the load vs strain curves reported in [39] for specimen JC2RF (see Fig. 23), the numerically predicted curves and experimental CFRP strains are found to be in a good agreement. It is important to note that all three specimens (JA2, JB2) tested in [39] produced a similar behaviour and a respective maximum reaction of approximately 58 to 59 kN. Similarly, JB2RF and JC2RF specimens gave a similar mechanical response in terms of hysteretic behaviour, while both specimens resulted in a maximum reaction of 120 kN, as reported in [39].

4.4 Computational Efficiency

Table 9 shows the computational demand for different parts of the analysis for the case of the JB2RF model. The total number of internal iterations that were performed during the cyclic nonlinear analysis was 5,513 and for their solution the developed algorithm required 323.9 seconds. This corresponds to a mere 0.059 seconds per internal iteration that characterizes the computational efficiency of the proposed modelling method.

Table 9 JB2RF Joint. Required computational time.

a/a	Description	Time (s)
1	Solution of 398 displacement increments	323.9

	(5,513 internal iterations)	
2	Computational Demand per internal iteration	0.059
3	Writing output file	140.7
4	Other	0.7
	Total	465.3

Fig. 24 shows the graph that correlates the obtained internal iterations per displacement increment in an attempt to further illustrate the excessive numerical nonlinearities that this type of problems develop during their cyclic analysis. As it can be observed, the number of internal iterations is relatively low for horizontally imposed displacements of less than 40 mm, where the average internal iteration per displacement increment is equal to 7.7. Whereas, when the drift becomes significant in the case of horizontal displacements that are beyond 40 mm, the number of required internal iterations per displacement increment are significantly larger. The average internal iterations per displacement increment in this case is 27.6, which highlights the extreme nonlinearities that occur within the model when the shear deformations are excessive.

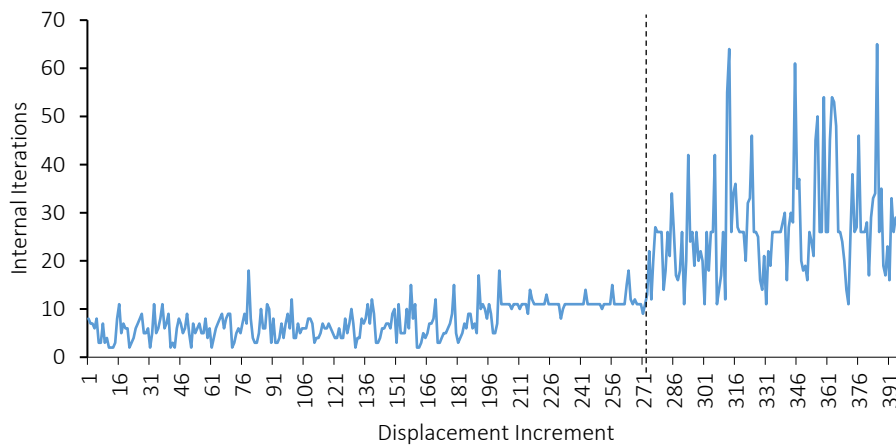


Figure 24: JB2FR Joint. Internal iterations vs displacement increment.

5. Conclusions and Future Work

A new damage factor that accounts for extreme nonlinearities caused by reinforcement bar slippage and excessive concrete cracking is introduced for capturing the mechanical behaviour of bare and retrofitted RC specimens that undergo ultimate limit state cyclic loading. Furthermore, a modification

of the concrete material constitutive matrix of crushed hexahedral GPs is proposed for inducing additional numerical stability in excessively cracked concrete regions that are subjected to cyclic loading conditions.

Based on the numerical findings, the proposed modelling method is found able to capture with acceptable accuracy the overall mechanical behaviour of both bare and retrofitted RC substructures subjected to extreme cyclic loading. This was achieved without the introduction of additional dofs or bond-slip models that would have complicated and slowed down the numerical procedure. In particular, the ability to capture the pinching effect and the mechanical response of rebars and CFRP sheets is demonstrated through the study of three joint specimens.

A further extension of this work is to study full-scale deficient RC structures under seismic loading, where an initial investigation is presented in [46]. Furthermore, the investigation of the numerical response of the developed model when combined with the HYMOD [2, 3] approach will be performed in the near future.

References

- [1] LONDON, Thomson Reuters Foundation, Timeline: World's 14 deadliest earthquakes of last decade, 13th November 13, 2017
<https://www.reuters.com/article/us-iran-quake-global/timeline-worlds-14-deadliest-earthquakes-of-last-decade-idUSKBN1DD257>
- [2] Markou, G. and Papadrakakis, M., (2015), “A Simplified and Efficient Hybrid Finite Element Model (HYMOD) for Non-Linear 3D Simulation of RC Structures”, *Engineering Computations*, 32 (5), pp. 1477-1524.
- [3] Markou, G., Mourlas, Ch., Bark, A. and Papadrakakis, M., (2018), “Simplified HYMOD Non-Linear Simulations of a Full-Scale Multistory Retrofitted RC Structure that Undergoes Multiple Cyclic Excitations – An Infill RC Wall Retrofitting Study”, *Engineering Structures*, Vol. 176, pp. 892–916..
- [4] Lykidis, G.Ch. and Spiliopoulos K.V. (2008), “3D solid finite element analysis of cyclically loaded RC structures allowing embedded reinforcement slippage”, *Journal of Structural Engineering-ASCE*, 134(4), 629-638.

- [5] Tedesco, J. W., Stallings J. M., and El-Mihilmy, M. (1999), "Finite Element Method Analysis of a Concrete Bridge Repaired with Fiber Reinforced Plastic Laminates," *Computers and Structures*, 72, 379-407.
- [6] Koteš P. and Kotula P. (2007), "Modeling and strengthening of RC bridges by means of CFRP", International Association of Fracture Mechanics for Concrete and Concrete Structures, FraMCoS-6 Catania, Italy, 2007 Proceedings, Paper 08-11.
- [7] Kachlakev D., Miller T., Yim S., Chansawat, K. and Tanarat P., Finite Element Modeling of Reinforced Concrete Structures Strengthened with FRP Laminates, Final Report for the Oregon Department of Transportation Research Group and Federal Highway Administration, 2001.
- [8] Niroomandi A., Maheri A., Maheri M. R. and Mahini S.S. (2010), "Seismic performance of ordinary RC frames retrofitted at joints by FRP sheets", *Engineering Structures*, 32(8), pp. 2326–2336
- [9] Anania L. and D'Agata G. (2013), "Numerical investigation on a new CFRP technology for the upgrading of the RC framed structures", Conference: ICCEN2014, Asia-Pacific Chemical, Biological & Environmental Engineering Society.
- [10] Arduini M., Di Tommaso A., and Nanni A. (1997), "Brittle Failure in FRP Plate and Sheet Bonded Beams," *ACI Structural Journal*, 94(4), pp. 363-370, 1997.
- [11] Godat A., Neale K. W. and Labossière P. (2007), "Numerical Modeling of FRP Shear-Strengthened Reinforced Concrete Beams", *Journal of Composites for Construction*, ASCE, 11(6), pp. 640-649.
- [12] Ibrahim A. M. and Mahmood M. Sh. (2009), "Finite Element Modeling of Reinforced Concrete Beams Strengthened with FRP Laminates", *European Journal of Scientific Research*, 30(4), pp. 526-541.
- [13] Chansawat K., Tanarat P., Miller T. H., Yim S. C. and Kachlakev D. I. (2009), "FE Models of GFRP and CFRP Strengthening of Reinforced Concrete Beams", *Advances in Civil Engineering*, volume 2009, pp. 1-13.
- [14] Shuraim A. B. (2011), "Efficacy of CFRP configurations for shear of RC beams: experimental and NLFE", *Structural Engineering and Mechanics*, 39(3), pp. 361-382.
- [15] Elsanadedy H. M., Almusallam T. H., Alsayed S. H. and Al-Salloum Y. A. (2013), "Flexural strengthening of RC beams using textile reinforced mortar – Experimental and numerical study", *Composite Structures*, 97, pp.40–55.

- [16] Duarte P., Correia J. R., Ferreira J. G., Nunes F. and Arruda M. R. T. (2014), "Experimental and numerical study on the effect of repairing reinforced concrete cracked beams strengthened with carbon fibre reinforced polymer laminates", *Canadian Journal of Civil Engineering*, 41, pp. 222–231.
- [17] Nasr Z. H., Alaa G. S., Amal H. Z. (2015), "Finite element analysis of reinforced concrete beams with opening strengthened using FRP", *Ain Shams Engineering Journal*,
<https://doi.org/10.1016/j.asej.2015.10.011>
- [18] Banjara N. K. and Ramanjaneyulu K. (2017), "Experimental and numerical investigations on the performance evaluation of shear deficient and GFRP strengthened reinforced concrete beams", *Construction and Building Materials*, 137, pp. 520–534.
- [19] Young-Min Y., Ashraf A., M. and Abdeldjelil B.F. (2011), "Three-Dimensional Nonlinear Finite-Element Analysis of Prestressed Concrete Beams Strengthened in Shear with FRP Composites", *Journal of Composites for Construction*, ASCE, 15(6), pp. 896-907
- [20] Qapo M., Dirar S., Yang J. and Elshafie M. Z. E. B. (2015), "Nonlinear finite element modelling and parametric study of CFRP shear-strengthened prestressed concrete girders", *Construction and Building Materials*, 76, pp. 245–255.
- [21] El-Hacha R., Zangeneh P. and Omran H. Y. (2012), "Finite Element Modeling of Steel-Concrete Composite Beams Strengthened with Prestressed CFRP Plate", *International Journal of Structural Stability and Dynamics*, 12(1), pp. 23-51.
- [22] Mostofinejad D. and Talaeitaba S. B. (2006), "Finite Element Modeling of RC Connections Strengthened with FRP Laminates", *Iranian Journal of Science & Technology, Transaction B, Engineering*, Vol. 30, No. B1, pp. 21-30.
- [23] Sinaei H., Jumaat M. Z. and Shariati M. (2011), "Numerical investigation on exterior reinforced concrete Beam-Column joint strengthened by composite fiber reinforced polymer (CFRP)", *International Journal of the Physical Sciences*, 6(28), pp. 6572-6579.
- [24] Sharma, A., Eligehausen, R., Reddy, G.R. (2011). "A new model to simulate joint shear behavior of poorly detailed beam-column connections in RC structures under seismic loads, part I: exterior joints". *Eng. Struct.* DOI: 10.1016/j.engstruct.2010.12.026.

- [25] Alhaddad M. S.; Siddiqui N. A.; Abadel A. A.; Alsayed S. H. and Al-Salloum Y. A. (2012), "Numerical Investigations on the Seismic Behavior of FRP and TRM Upgraded RC Exterior Beam-Column Joints", *Journal of Composites for Construction*, 16(3), pp. 308-321.
- [26] Dalalbashi A., Eslami A. and Ronagh H. R. (2013), "A numerical investigation on the hysteretic behavior of RC joints retrofitted with different CFRP configurations", *Journal of Composites for Construction*, 17(3), pp. 271-382.
- [27] Sharma, A., Eligehausen, R, Hofmann, J (2014). "Numerical modeling of joints retrofitted with haunch retrofit solution". *ACI Structural Journal*, 111(4), 861-72.
- [28] Azarm R., Maheri M. R. and Torabi A. (2016), "Retrofitting RC Joints Using Flange-Bonded FRP Sheets", *Iranian Journal of Science and Technology, Transactions of Civil Engineering*, 41(1), pp 27–35.
- [29] Elsanadedy H. M., Al-Salloum Y. A., Alsayed S. H. and Iqbal R. A. (2012), "Experimental and numerical investigation of size effects in FRP-wrapped concrete columns", *Construction and Building Materials* 29, pp. 56–72.
- [30] Mazzucco G., Salomoni V. A., Majorana C. E., Pellegrino C. and Ceccato C. (2016), "Numerical investigation of concrete columns with external FRP jackets subjected to axial loads", *Construction and Building Materials*, 111, pp. 590–599.
- [31] M. Chellapandian, S. Suriya Prakash, Vinay Mahadik, and Akanshu Sharma (2020). "Microplane-based nonlinear finite element analysis of fiber-reinforced polymer-strengthened reinforced concrete columns". *ACI Structural Journal*, 117(1). DOI: 10.14359/51718075
- [32] Milani G. and Lourenço P. B. (2013), "Simple Homogenized Model for the Nonlinear Analysis of FRP-Strengthened Masonry Structures. II: Structural Applications", *Journal of Engineering Mechanics, ASCE*, 139(1), pp. 77-93.
- [33] Mrozek M., Mrozek D. and Wawrzynek A. (2015), "Numerical analysis of selection of the most effective configuration of CFRP composites reinforcement of masonry specimens", *Composites Part B: Engineering*, 70, pp. 189–200.
- [34] Gribniak V., Arnautov A. K., Kaklauskas G., Jakstaite R., Tamulenas V. and Gudonis E. (2014), "Deformation Analysis of RC Ties Externally Strengthened with FRP Sheets", *Mechanics of Composite Materials*, 50(5), pp. 669-676.

- [35] Cortés-Puentes W. L. and Palermo D. (2012), “Modeling of RC Shear Walls Retrofitted with Steel Plates or FRP Sheets”, *Journal of Structural Engineering*, ASCE, 138(5), pp. 602-612.
- [36] Mourlas, C., Markou, G. and Papadrakakis, M. (2019), “Accurate and Computationally Efficient Nonlinear Static and Dynamic Analysis of Reinforced Concrete Structures Considering Damage Factors”, *Engineering Structures*, 178 (2019), pp. 258–285.
- [37] Markou G., Papadrakakis M. (2013), “Computationally efficient 3D finite element modeling of RC structures”, *Computers and Concrete*, 12(4), 443–98.
- [38] Mourlas, Ch., Papadrakakis M. and Markou, G. (2017), “A Computationally Efficient Model for the Cyclic Behavior of Reinforced Concrete Structural Members”, *Engineering Structures*, 141, pp. 97–125.
- [39] Garcia, R., Jemaa, Y., Helal; Y., Guadagnini, M. and Pilakoutas, K. (2014), “Seismic Strengthening of Severely Damaged Beam-Column RC Joints Using CFRP”, *Journal of Composites for Construction*, 18(2), 04013048.
- [40] Kotsovos M.D. and Pavlovic M.N. (1995), *Structural concrete. Finite Element Analysis for Limit State Design*, Thomas Telford, London.
- [41] Willam K. J. and Warnke E. P., (1974), “Constitutive model for the triaxial behaviour of concrete”, Seminar on concrete structures subjected to triaxial stresses, Instituto Sperimentale Modelli e Strutture, Bergamo, Paper III-1.
- [42] Menegotto, M., and Pinto, P. E. (1973). “Method of analysis for cyclically loaded reinforced concrete plane frames including changes in geometry and non-elastic behavior of elements under combined normal force and bending.” *Proceedings, IABSE Symposium on Resistance and Ultimate Deformability of Structures Acted on by Well Defined Repeated Loads*, Lisbon, Portugal, 15–22.
- [43] Markou, G., AlHamaydeh, M. (2018), 3D Finite Element Modeling of GFRP-Reinforced Concrete Deep Beams without Shear Reinforcement, *International Journal of Computational Methods*, 15(1), pp. 1-35.
- [44] Markou, G., Mourlas, C. and Papadrakakis, M. (2017), “Cyclic Nonlinear Analysis of Large-Scale Finite Element Meshes Through the Use of Hybrid Modeling (HYMOD)”, *International Journal of Mechanics*, 11(2017), pp. 218-225.
- [45] Reonan FEA v2.00, User’s Manual, 2020.
https://www.researchgate.net/publication/342361609_ReConAn_v200_Finite_Element_Analysis_Software_User's_Manual

- [46] Markou, G. (2021), A New Method of Seismic Retrofitting Cost Analysis and Effectiveness for Reinforced Concrete Structures, *Engineering Structures*, 246 (2021), 113083.